Supporting Information

Emma A. Petersen-Sonn[1], Marcello Brigante[2], Laurent Deguillaume[3,4], Jean-Luc Jaffrezo[5], Sébastien Perrier[1], and Christian George[1]*

[1]Universite Claude Bernard Lyon 1, CNRS, IRCELYON, UMR 5256, Villeurbanne, F-69100

[2]Université Clermont Auvergne, CNRS, Institut de Chimie de Clermont-Ferrand, F-63000, Clermont-Ferrand, France

[3]Université Clermont Auvergne, CNRS, Laboratoire de Météorologie Physique, Clermont-Ferrand, France

[4]Université Clermont Auvergne, CNRS, Observatoire de Physique du Globe de Clermont Ferrand, Clermont-Ferrand, France

[5]Université Grenoble Alpes, CNRS, IRD, Grenoble INP, INRAE, Institut des Géosciences de l'Environnement, Grenoble, 38400, France

1. Hydroxyl radical formation measured by 2-hydroxyterephthalic acid fluorescence

Fluorescence spectra were recorded every 5-10 min, during 40-60 minutes of irradiation. The TAOH formation curves for the experiments are shown in Figure S16-19. By applying the TAOH calibration curves it was possible to follow the formation of TAOH with time. Linear regressions were performed on these curves to obtain the rate of TAOH formation derived from the slope. Charbouillot et al. (2011)[1] presented a yield of OH formation from TAOH dependent on the pH, which allowed the calculation of OH formation as seen in Equation S1.

$$\Gamma_{TAOH} = (0.0248 \pm 0.0059)\, pH + (0.046 \pm 0.035) \qquad \text{(S1)}$$

The pH in the solutions 5.7 and 6.7 in the VL experiments. In nitrate solutions, the pH was between 6.4 and 7.0, while for hydrogen peroxide the range was from 6.2 to 6.4. These differences in pH was considered by means of Equation S1, that was used to calculate the yield TAOH from each individual experiment. The slope of the linear fit of [TAOH] vs time of the different OH source concentrations was divided by the yield of OH formation (Eq. S1) , leading to figures S9-11. These plot shows the OH formation rate as a function of the compounds. From the linear regression of this curve, the slope (and its variability) is found, resulting in a value for the OH formation rate depending on the species concentration (in units of M s^{-1} $M(comp)^{-1}$). This method for estimating the OH formation rates was applied to vanillin and 4HB, as well as two other sources of OH in the aqueous phase, NO_3^- and H_2O_2.

2. Aerosol samples

The sampling dates of the samples were 29/11/2021 to 02/12/2021 for the sample referred to as 021221, and 13/12/2021 to 14/12/2021 for the sample referred to as 141221. The dissolved organic carbon of the samples was analyzed as described in the main text and the resulting values were

73.42 and 64.01 mgC L^{-1} for the 021221 and 141221 samples, respectively. Blank filter extractions are regularly performed to track the extraction performance. Eventually, some simple carboxylic acids are reaching mg levels, while most complex organics were below the detection limit at tens of µg levels. This contamination represents a very small fraction of the organics present during our experiments.

3. Degradation of the triplet state probe, TMP

The triplet state steady-state concentration was estimated by using TMP with UPLC/UV detection. The degradation of TMP gave a first-order rate constant ($k_{obs,TMP}$), that similarly to singlet oxygen can be applied in calculation the steady-state concentration. Although TMP is common probe for triplet states, it can also be degraded by singlet oxygen and OH radicals. Therefore, $k_{obs,TMP}$ should be corrected for the influence of singlet oxygen, OH radicals, and also direct photolysis ($k_{blank,TMP}$). The steady-state concentrations of singlet oxygen and OH radicals in the two samples were estimated from previous experiments with the same sample extracts but slightly varying conditions (20 °C, 20 mL reactor). The singlet oxygen concentrations were determined to be $(5.17 \pm 0.23) \times 10^{-13}$ and $(5.59 \pm 0.26) \times 10^{-13}$ M for samples 02122021B and 141221B, respectively. The steady-state OH radical concentrations were calculated as described in section S4.

An average second-order rate constant between TMP and triplet states ($k_{3C*,TMP}$) from a variety of sources (listed in the Table S1) was calculated to be $(1.46 \pm 1.17) \cdot 10^9$ M^{-1} s^{-1}. Using this second-order rate constant of TMP with triplets, along with the second-order rate constant for TMP with singlet oxygen ($k_{1O2,TMP}$) and with OH radicals ($k_{OH,TMP}$), the steady-state triplet state concentrations are calculated as:

$$[^3C^*]_{ss} = \frac{k_{obs,TMP} - (k_{blank,TMP} + k_{1O2,TMP}[^1O_2]_{ss} + k_{OH,TMP}[OH]_{ss})}{k_{3C*,TMP}} \quad \text{(S2)}$$

The value for $k_{OH,TMP}$ was an average value of the reaction of OH radicals with 2-methylphenol and 4-methylphenol [2], because no value for the rate constant of TMP and OH radicals was found.

When the steady-state triplet state concentrations of the photosensitizers were estimated, the concentrations were calculated as a simplified version of Equation S2, where the correction for singlet oxygen and OH radical interference with the probe was omitted.

Table S1. Second-order rate constants between triplet states and TMP. CDOM: chromophoric dissolved organic matter.

Triplet state source	**$k_{3C*,TMP}$ (10^9 M^{-1} s^{-1})**	**Refence**
2-acetonaphthone	0.617 ± 0.016	Wenk 2013 [3]
2-acetonaphthone	0.72 ± 0.01	Canonica 2000 [4]
3-methoxyacetophenone	1.88 ± 0.21	Wenk 2013 [3]
3-methoxyacetophenone	2.6 ± 0.3	Canonica 2000 [4]
4-carboxybenzophenone	3.3 ± 2.4	McCabe & Arnold 2017 [5]
Benzophenone	5.1 ± 0.9	Canonica 2000 [4]
CDOM (Canal)	3.0 ± 1.1	al Housari 2009 [6]
CDOM (Vaccarès)	4.8 ± 4.4	al Housari 2009 [6]
DOM (Great Dismal Swamp)	0.77 ± 0.01	Erickson 2018 [7]
DOM (Lake Bradford)	0.84 ± 0.03	Erickson 2018 [7]
Fulvic acid (Pony Lake)	1.26 ± 0.02	Erickson 2018 [7]
Fulvic acid (Suwannee River)	0.54 ± 0.01	Erickson 2018 [7]
Humic acid (Suwannee River)	0.75 ± 0.03	Erickson 2018 [7]
NOM (Mississippi River)	0.90 ± 0.02	Erickson 2018 [7]
NOM (Suwannee River)	0.63 ± 0.02	Erickson 2018 [7]
Watershed (CMH07)	1.4 ± 0.4	McCabe & Arnold 2017 [5]

Watershed (CMH07)	2.0 ± 0.5	McCabe & Arnold 2017 [5]
Watershed (H2)	1.7 ± 0.3	McCabe & Arnold 2017 [5]
Watershed (H2)	1.7 ± 0.6	McCabe & Arnold 2017 [5]
Watershed (KC)	2.2 ± 0.5	McCabe & Arnold 2017 [5]
Watershed (KC)	2.0 ± 0.3	McCabe & Arnold 2017 [5]
Watershed (KC)	2.1 ± 1.2	McCabe & Arnold 2017 [5]
Watershed (TBO)	1.5 ± 0.6	McCabe & Arnold 2017 [5]

3.1 Probe control experiments

Various probe molecules, including TMP, sorbic acid, but also other dienes have been used to indirectly assess and quantify different triplet states. It is important to note that these probes, such as TMP and sorbic acids, quantify distinct triplet pools, differing in quantity and reactive nature[8]. TMP is directly oxidized by organic matter triples states while dienes primarily engage through energy transfer, targeting high-energy triplets. When energy transfers to a diene occur, they generate triplet excited dienes, then probably secondary reactivities in water. We opted for TMP in our study due to its stability in aqueous solution and simple and rapid detectability through

High-Performance Liquid Chromatography (HPLC) analysis in complex media.

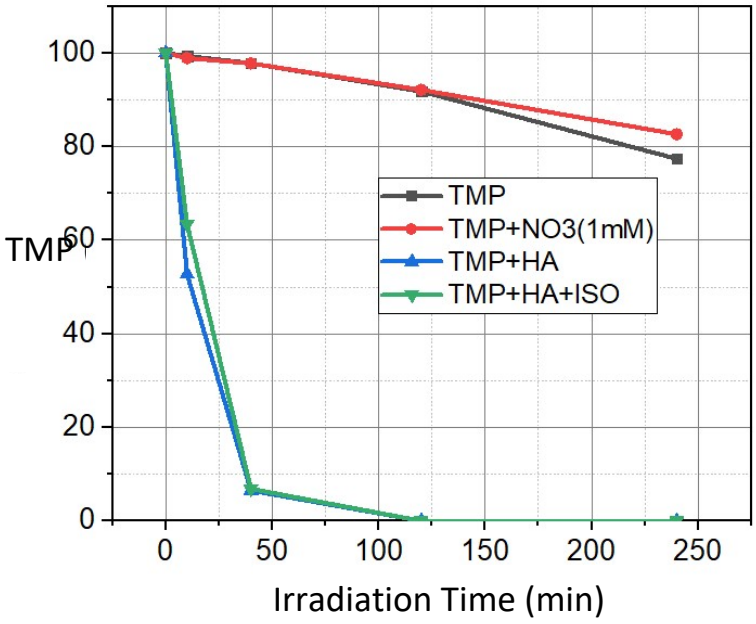

Figure S1. TMP degradation (in pct) by photolysis (black), nitrate (red), humic acid (blue), and humic acid and isopropanol (green).

In order to assess the direct oxidation of TMP by hydroxyl radicals, we conducted additional experiments where the concentration of TMP was monitored in the presence of nitrate ions (NO_3^-) under photolysis (serving as a source of hydroxyl radicals) and humic acids (HA), known to generate excited states with and without isopropanol (ISO), a recognized hydroxyl radical scavenger (Figure S1).

Figure S1 illustrates that, after 3 hours of irradiation, there was no significant enhancement in TMP degradation, with approximately 20% of TMP undergoing degradation via direct photolysis. However, in the presence of HA, there was a marked increase in TMP degradation (which is expected due to the formation and then reactivity with excited states). Notably, the use of

isopropanol did not alter this degradation, suggesting that isopropanol had no direct effect on the reactivity of the triplet states with TMP.

To test the effect of singlet molecular oxygen, an experiment with TMP+VL was performed with nitrogen to remove the molecular oxygen from the solution. N_2 was bubbled through the solution for 40 min (in the dark) before the start of the irradiation. Hereafter, the irradiation was started while nitrogen continued to be bubbled through the solution. An experiment with a standard TMP+VL solution was performed on the same day. Both experiments were performed in the glass reactor at 15 °C, similar to the experiments containing TMP described in the main text. The concentration of both compounds was 100 µM. The TMP was detected by UHPLC/UV detection (described in section S3.2). The results are shown in Figure S2.

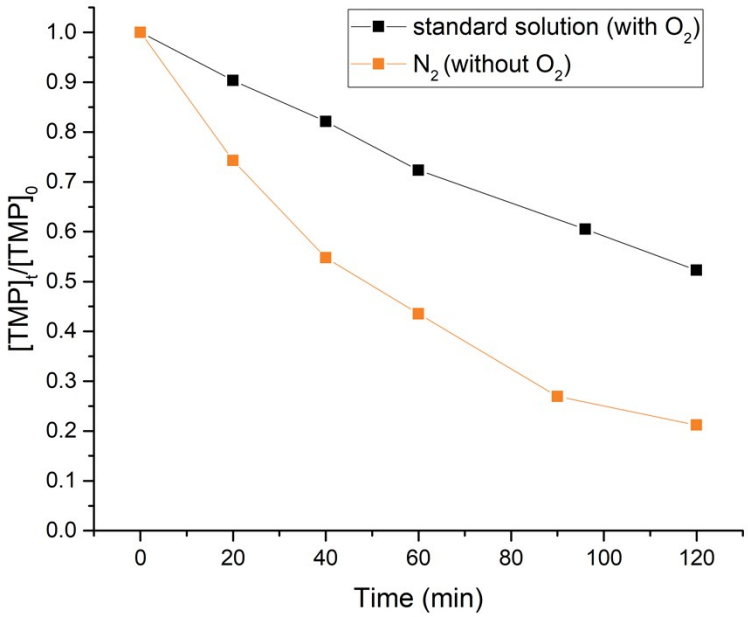

Figure S2. Degradation of TMP (100 µM) with VL (100 µM) in a standard solution (containing O2, black) and in a solution that had been bubbled with nitrogen (without O2, orange).

The results of these experiments showed that the degradation of TMP was faster in the N_2 (without O_2) solution than in the standard solution (with O_2). This indicates that singlet oxygen does not have a significant effect on the degradation of TMP. It is possible that the faster degradation of TMP in an N_2 solution is due to less quenching of the triplet states by O_2 (i.e. because most O_2 is removed from the solution).

In this study, aerosol samples were collected and extracted as described in the main text. These samples were extracted for brown carbon, and hereby represent an aerosol constituent responsible for a large amount of triplet state formation. The degradation of TMP by the BrC extracts was compared to that of VL. This gives an indication of whether VL can be regarded as a proxy for aerosol components.

3.2 Experimental set-up

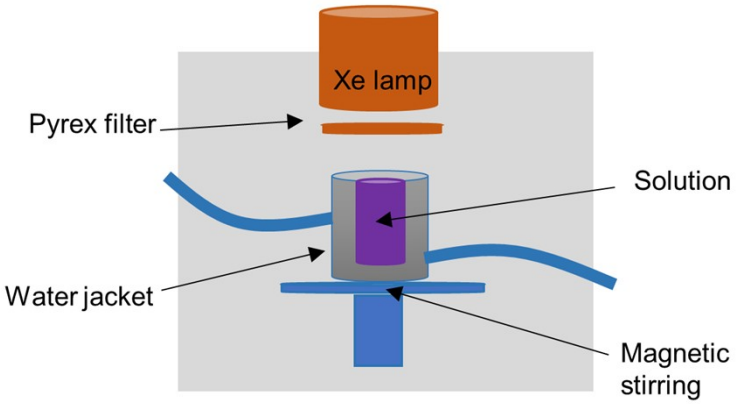

In this section, a sketch of the experimental set-up for the degradation of TMP is shown. This set-up was also applied for analyzing the TAOH formation from the aerosol samples as described in the following section (S3.2).

3.3 Method for U(H)PLC/UV and UPLC/FLR analysis

The samples for the experiments regarding the degradation of TMP (described in the main text) were analyzed in the UPLC with UV detection. The method consisted of a flow of 0.6 ml/min with 95 % water (with 1% H_3PO_4) and 5 % methanol (ultrapure, UPLC grade) for the initial 0-4.5 min. Hereafter, the solvents were changed to have 5 % water (with 1% H_3PO_4) and 95 % methanol until 5.1 min, where after the method returned to 95 % water (with 1% H_3PO_4) and 5 % methanol (ending at 6 min).

UHPLC/UV detection for the TMP control experiments (with VL in O_2 or N_2) was performed with an ACQUITY UPLC HSS T3 by WATERS column (100 mm x 2.1 mm, 1.8µm particle size). The flow through the UHPLC was 0.3 mL/min and consisted of solvent A: H_2O with 0.1% formic acid, and/or solvent B: ACN with 0.1% formic acid. The gradient was as follows; 0-2 min: 1% solvent B and 99% solvent A, 2-13 min: the solvent changed gradually from 1 to 100% B (with solvent A as the remaining), 13-15 min: the solvent remained 100% B, 15-15.1 min: the solvent gradually changed from 100 to 1% solvent B (with solvent A as the remaining), 15.1-22 min: the solvent remained 1% B and 99% solvent A.

The OH steady-state concentration was determined for the two aerosol samples by applying terephthalic acid as a probe and analyzing the TAOH formation by UPLC with fluorescence detection. In the experiments the sample concentration was 10 mgC/L, and the TA concentration was 500 µM. A 50 ml reactor was used and the samples were irradiated for 60 min, using the same set-up as for the TMP experiments. The TA concentration was higher in these experiments compared to those performed with the other OH sources (ie. VL, H_2O_2, and NO_3^-) because we needed a TAOH concentration that was sufficient for detection by UPLC/FLR. The method for this analysis had a flow of 0.6 ml/min and began with 95 % water (with 1% H_3PO_4) and 5 %

methanol (ultrapure, UPLC grade) from 0 min to 4.5 min. From 4.5 to 5 min, the solvent changed to 40 % water (with 1% H_3PO_4) and 60 % methanol and remained at this ratio until 5.1 min, where after it was changed back to 95 % water (with 1% H_3PO_4) and 5 % methanol. The method had a duration of 6 min.

4. OH steady-state concentrations

The calculations of the OH steady-state concentrations of in the various experiments were performed by the following equation, put forth by Lallement et al.[9];

$$[OH]_{ss} = \frac{k_{obs}}{\gamma_{TAOH} \cdot k_{TA,OH} \cdot [TA]} \quad \text{(S3)}$$

Where k_{obs} is the first-order rate constant for the formation of TAOH, γ_{TAOH} is the yield of formation of TAOH, $k_{TA,OH}$ is the second-order rate constant between TA and OH radicals, and [TA] is the concentration of TA.

The steady-state concentrations of OH for the applied sources of OH radicals can be found in Figures S3-6. The TAOH formation for all species is shown in Figures S16-20.

The $[OH]_{ss}$ was also determined in blank experiments with TA as described in section 3.2 (SI).

Table S2. OH steady-state concentrations. For nitrate anions, hydrogen peroxide, and VL, a range of concentrations are giving, indicating the minimum and the maximum concentration.

Compound	*$[OH]_{ss}$ (M)*
NO_3^-	$(1.10 \pm 0.62) \cdot 10^{-16}$ to $(4.81 \pm 1.6) \cdot 10^{-15}$
H_2O_2	$(5.15 \pm 0.97) \cdot 10^{-16}$ to $(7.31 \pm 1.5) \cdot 10^{-15}$
VL	$(8.67 \pm 1.9) \cdot 10^{-17}$ to $(6.20 \pm 2.6) \cdot 10^{-16}$
4HB	$(8.34 \pm 0.27) \cdot 10^{-17}$ to $(1.48 \pm 0.064) \cdot 10^{-16}$

021221	$(2.10 \pm 0.53) \cdot 10^{-16}$
141221	$(1.88 \pm 0.45) \cdot 10^{-16}$
blank ([TA] = 500µM)	$(7.0 \pm 1.86) \cdot 10^{-18}$

5. Figures

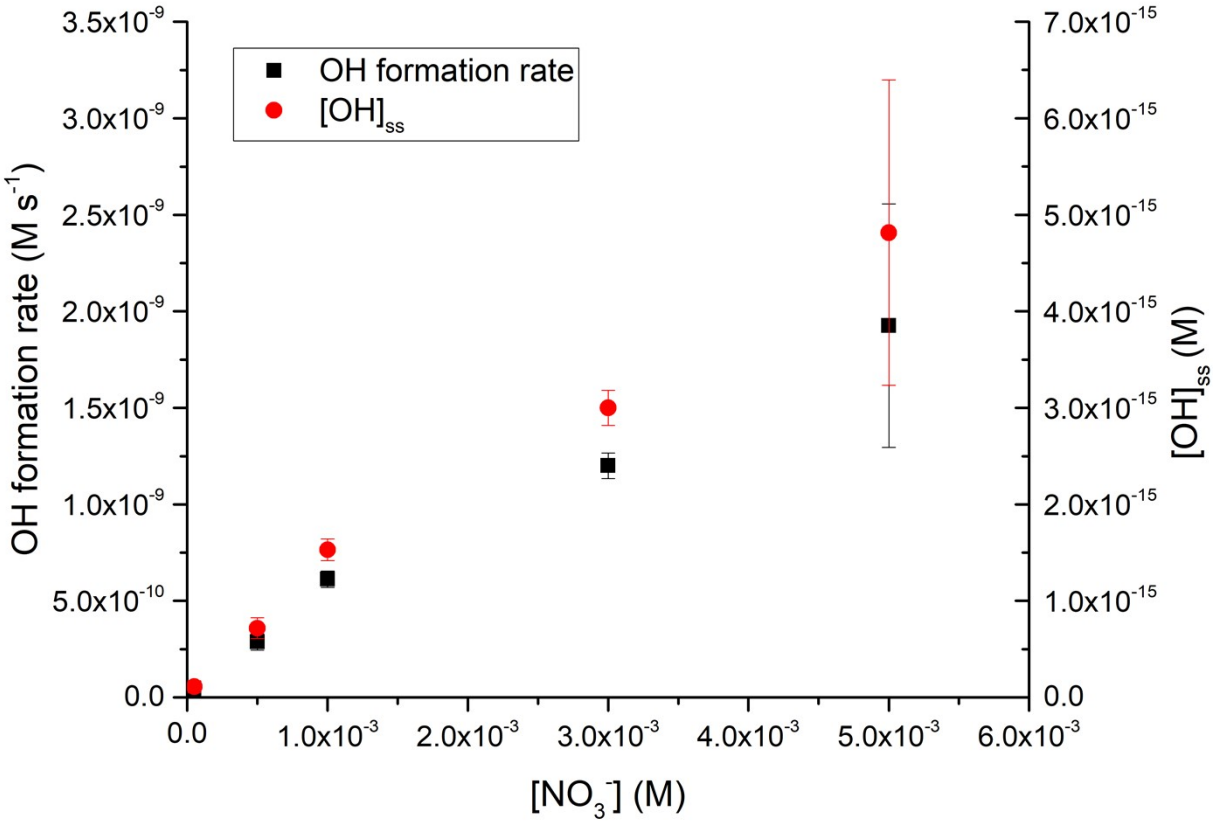

Figure S3. OH formation rate (black squares) and OH steady-state concentrations (red circles) for nitrate anions.

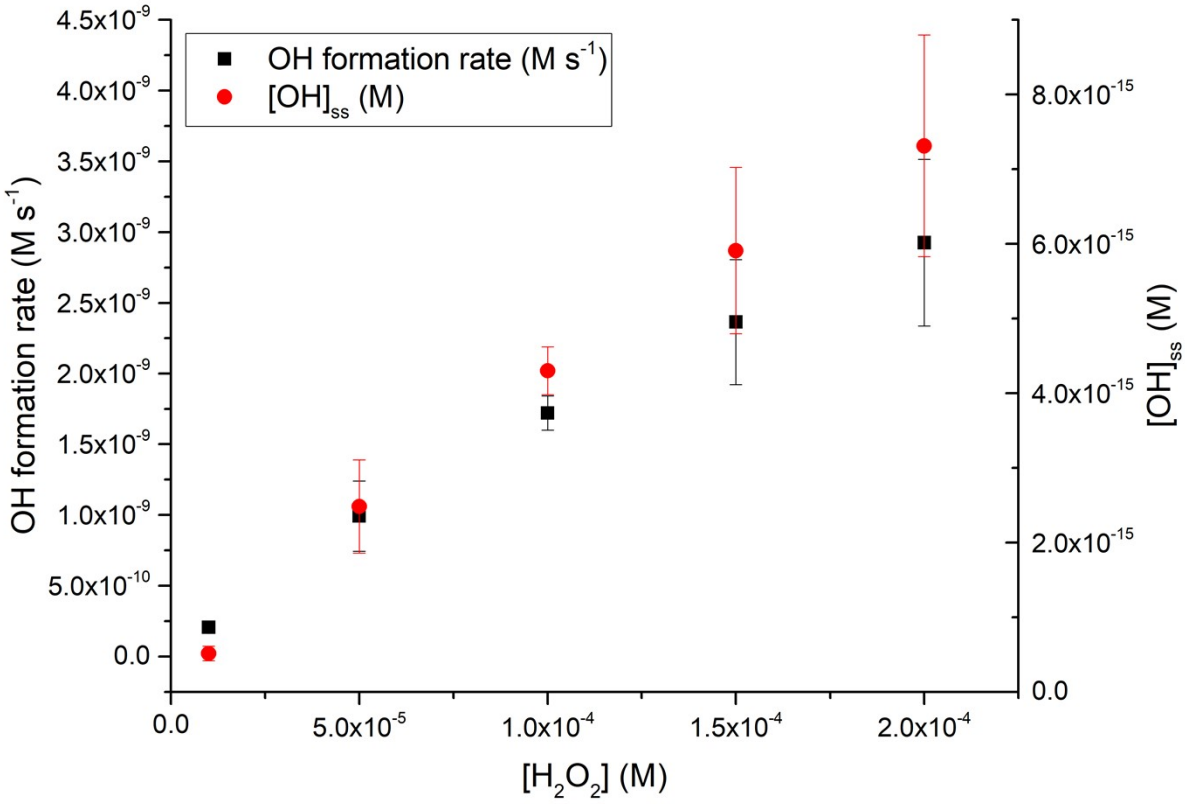

Figure S4. OH formation rate (black squares) and OH steady-state concentrations (red circles) for hydrogen peroxide.

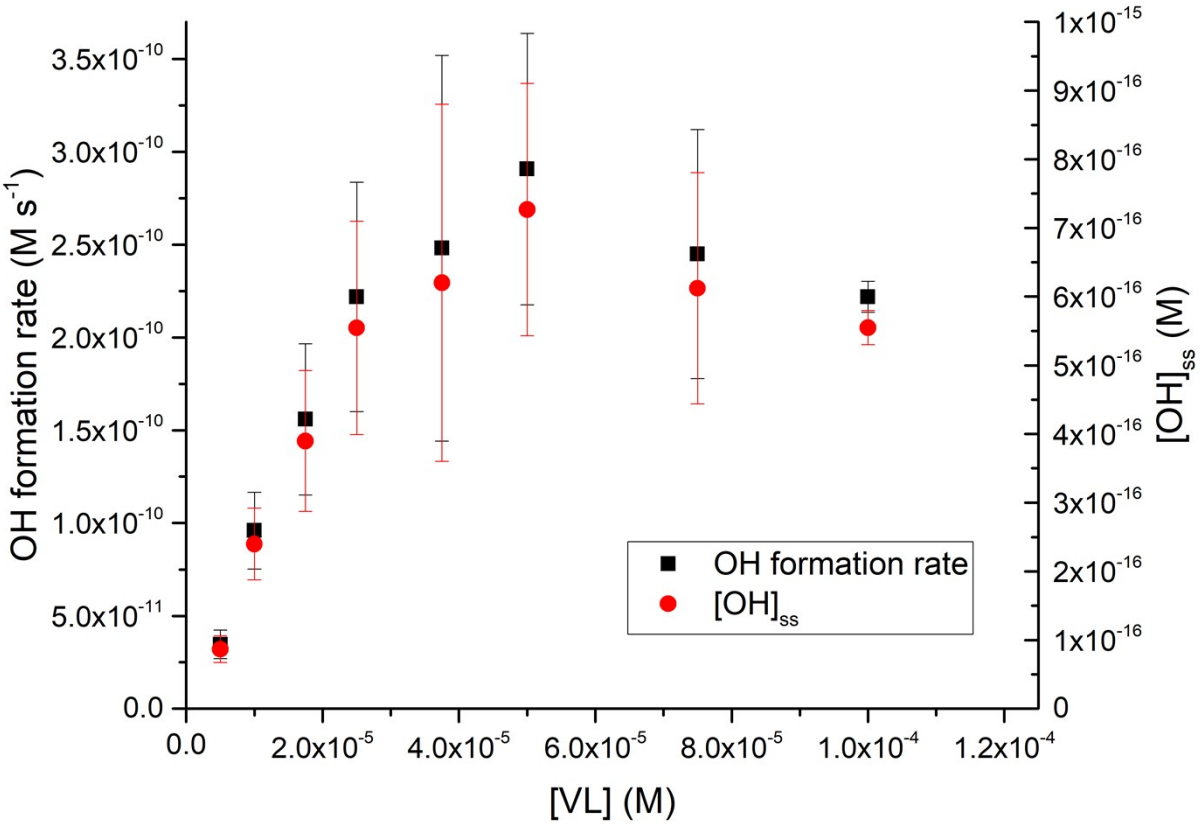

Figure S5. OH formation rate (black squares) and OH steady-state concentrations (red circles) for VL.

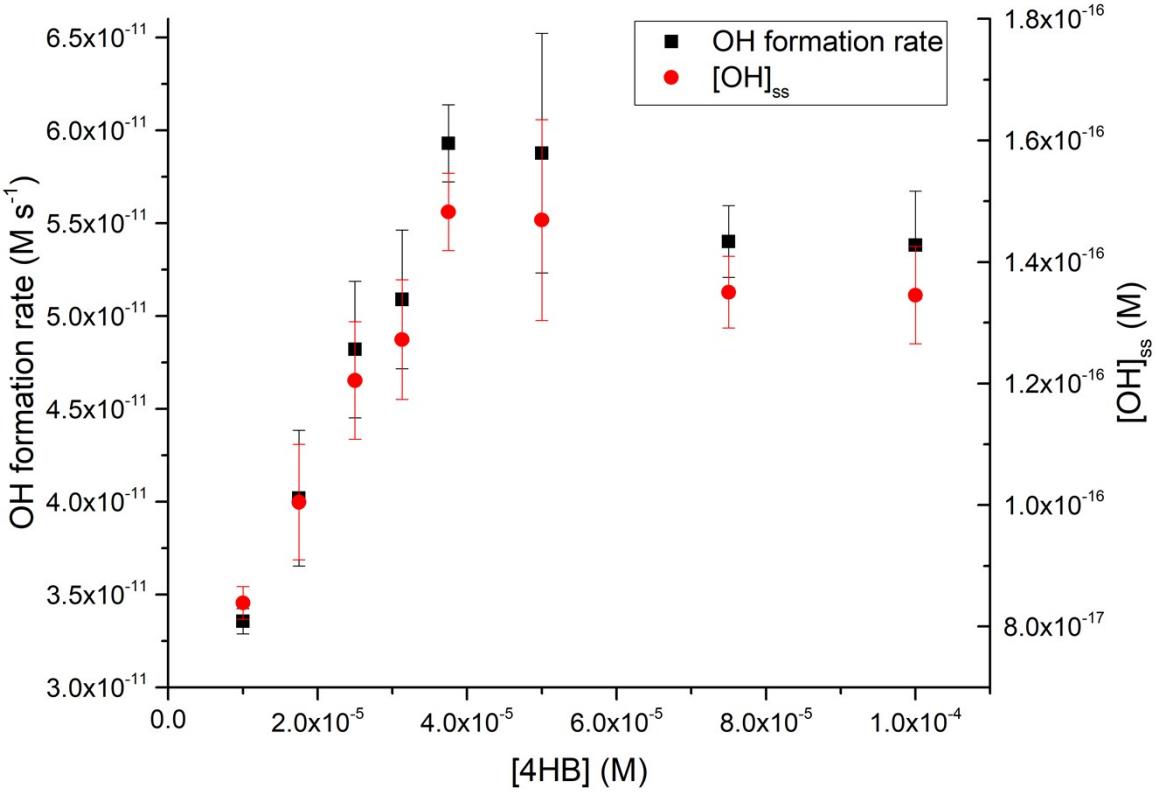

Figure S6. OH formation rate (black squares) and OH steady-state concentrations (red circles) for 4HB.

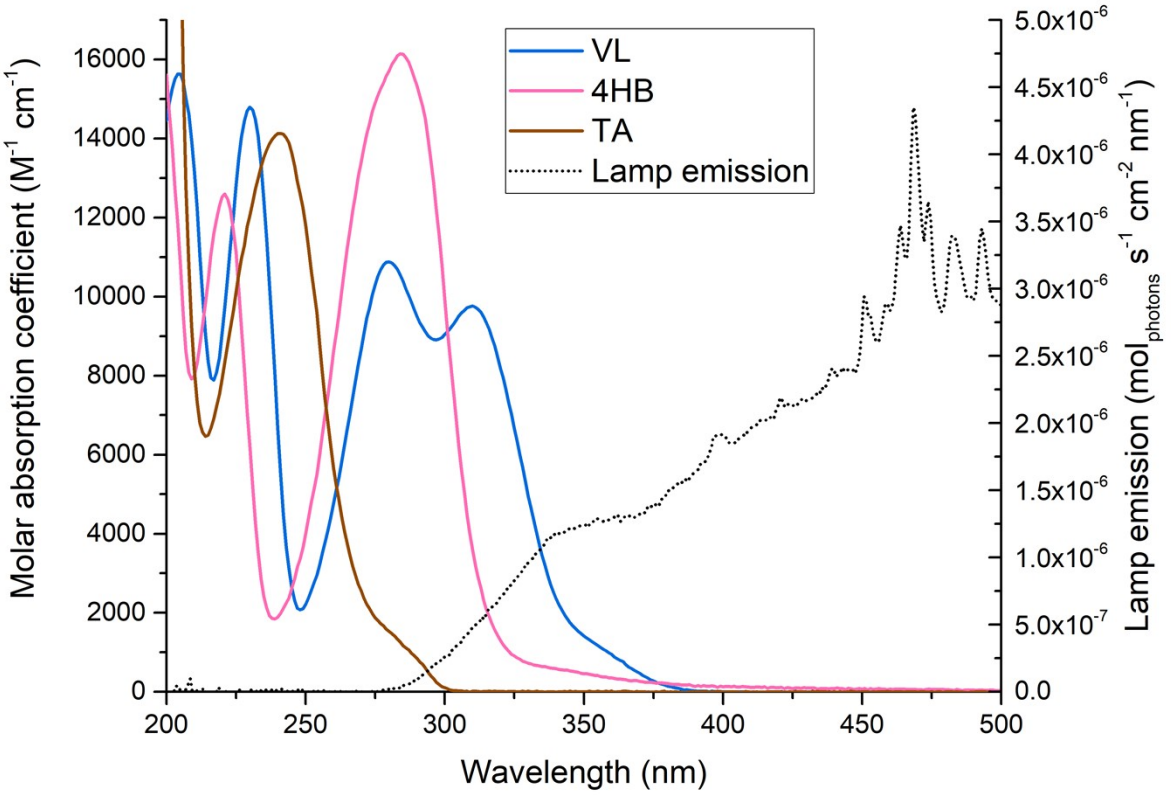

Figure S7. Emission of the Xenon lamp (dotted black line, right y-axis), and molar absorption coefficients (left y-axis) of VL (blue, full line), 4HB (pink, full line), and TA (brown, full line).

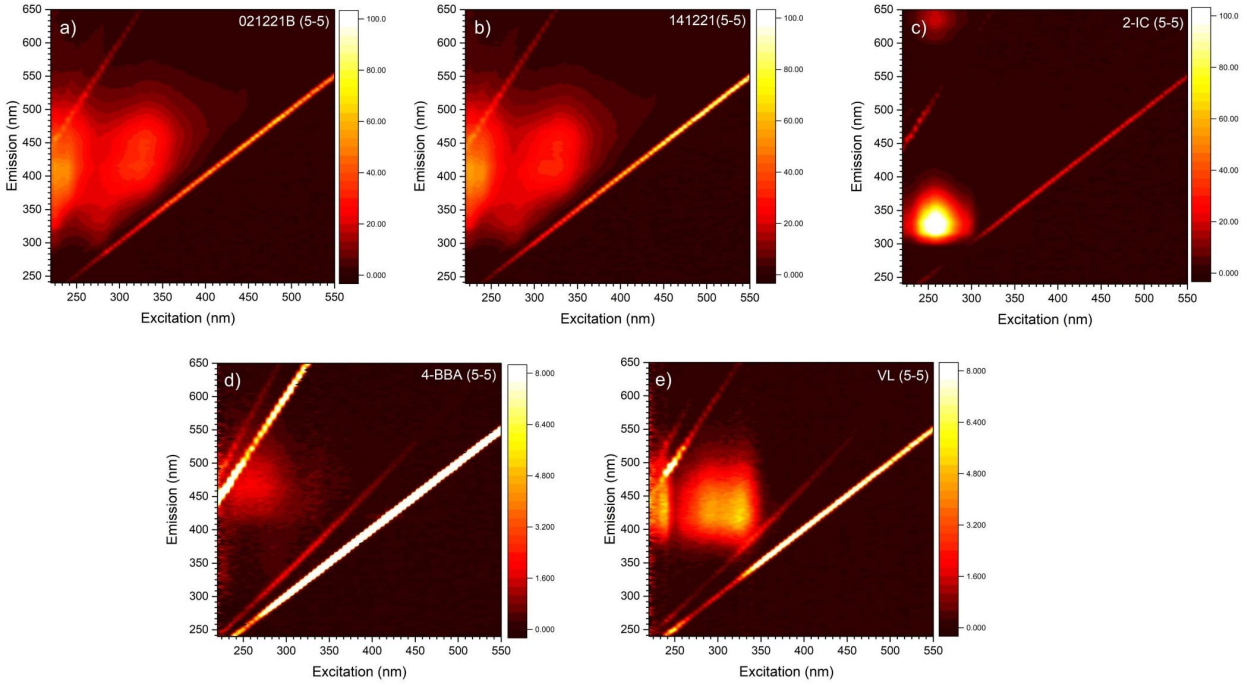

Figure S8. Excitation emission matrix (EEM) spectra of the samples 021221 (a) and 141221 (b), and the three photosensitizers, 2-IC (c), 4-BBA (d), and VL (e). The color bars denote the fluorescence intensity (a.u.). All spectra were performed with slits of 5 nm for both excitation and emission. Note the difference in intensity scale of the fluorescence; the top row (a-c) share a scale with a maximum of 100, while the bottom row (d-e) share a scale with a maximum of 8.

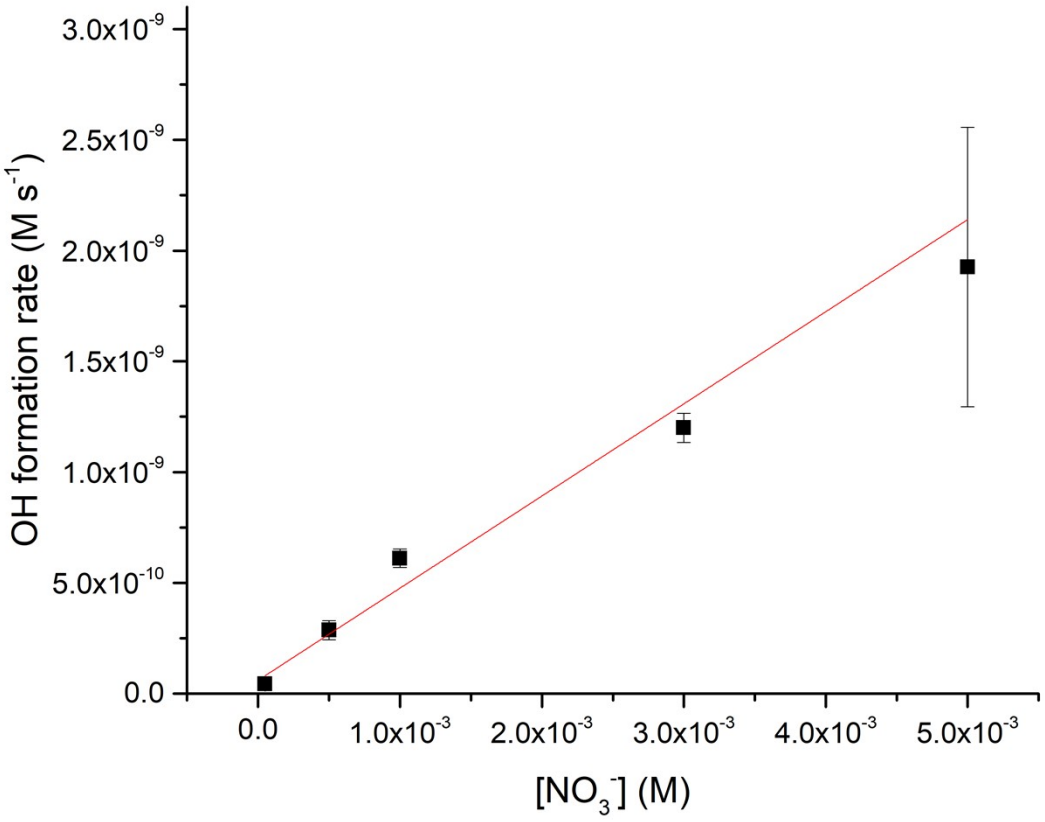

Figure S9. OH formation rates from nitrate anions. A linear fit is applied and the resulting slope is $(4.16 \pm 0.51) \times 10^{-7}$ M s^{-1} M$(NO_3^-)^{-1}$. The points are results of duplicate experiments.

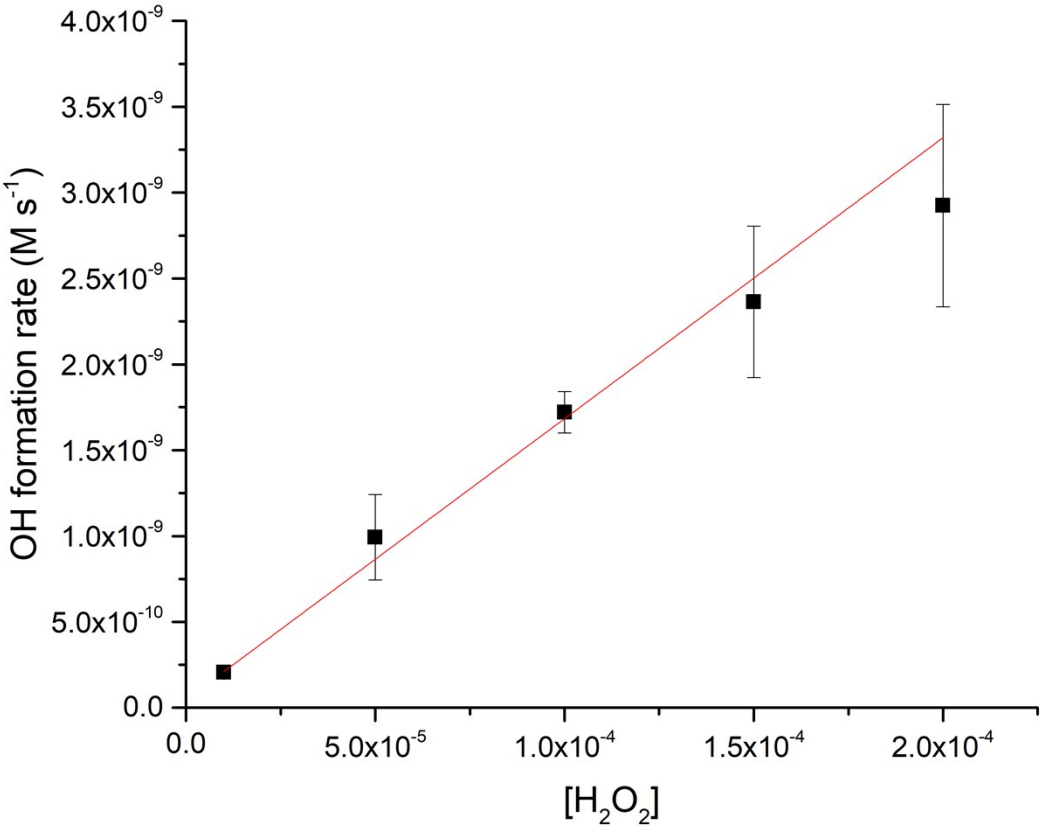

Figure S10. OH formation rate of H_2O_2. A linear fit is applied and the resulting slope (1.64 ± 0.06) × 10^{-6} M s^{-1} $M(H_2O_2)^{-1}$. The points are results of duplicate experiments.

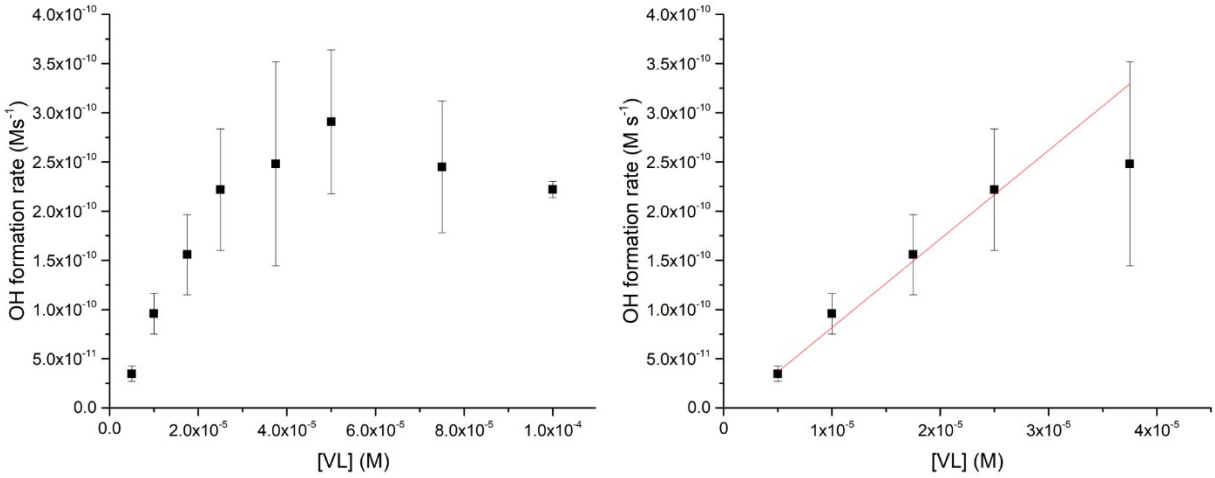

Figure S11. OH formation rate of VL. The left figure shows the whole plot (each point is the result

of triplicate experiments), while the right figure shows the linear fit that is applied to points from 5×10^{-5} to 3.75×10^{-4} M. The slope of the linear regression is 9.00×10^{-6} M s^{-1} $M(VL)^{-1}$.

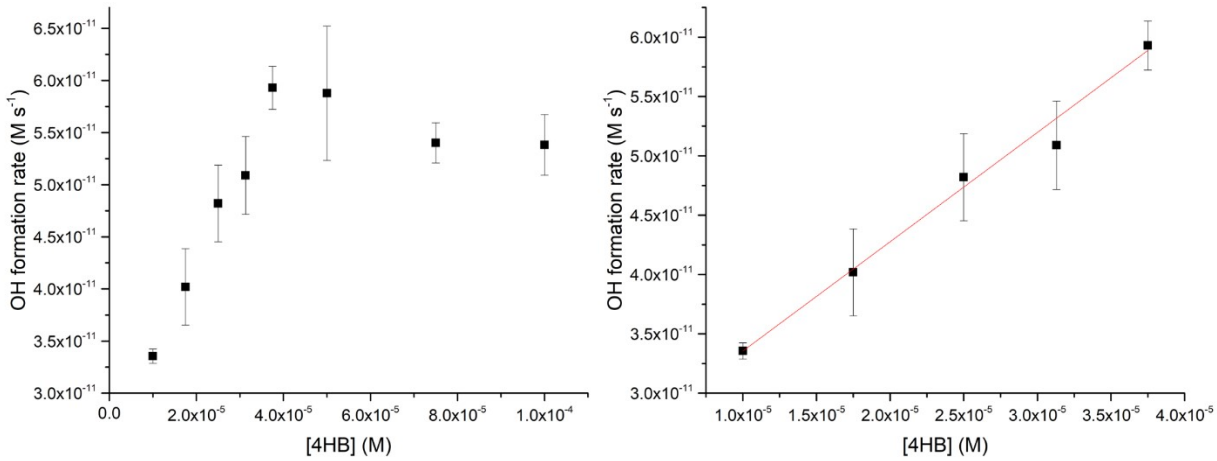

Figure S12. OH formation rate of 4HB. The left figure shows the whole plot, while the right figure shows the linear fit that is applied to points from 5×10^{-5} to 3.75×10^{-4} M. The slope of the linear regression is $(9.21 \pm 0.28) \times 10^{-7}$ M s^{-1} $M(4HB)^{-1}$. The points applied in the linear regression is the results of triplicate experiments, while the three points at higher concentrations are from duplicate experiments.

6. OH formation rates in literature

In Table S3, literature values for OH formation rates are shown in various environments.

Table S3. OH formation rates from literature studies on aerosols or cloud/fog.

Reference	*Type*	*Location*	*OH formation rate (M s^{-1})*
Anastasio et Jordan 2004 [10]	Arctic particles	Nunavut, Canada	$2.8 \cdot 10^{-12}$ to $3.0 \cdot 10^{-9}$
Anastasio et McGregor 2001 [11]	Fog	California, USA	$2.4 \cdot 10^{-10}$ to $1.9 \cdot 10^{-9}$

Anastasio et Newberg 2007 [12]	Sea salt particles	Coast of California, USA	$1.0 \cdot 10^{-8}$ to $2.3 \cdot 10^{-6}$
Arakaki 2006 [13]	Particle extracts	Okinawa, Japan	$7.3 \cdot 10^{-11}$ to $3.8 \cdot 10^{-10}$
Arakaki et Faust 1998 [14]	Cloud	New York, USA	$3.3 \cdot 10^{-11}$ to $5.2 \cdot 10^{-10}$
Bianco 2015 [15]	Cloud (experimental)	Puy de Dôme, France	$1.1 \cdot 10^{-11}$ to $4.2 \cdot 10^{-10}$
Bianco 2015 [15]	Cloud (modelled)	Puy de Dôme, France	$1.1 \cdot 10^{-11}$ to $2.4 \cdot 10^{-10}$
Faust et Allen 1993 [16]	Cloud/fog	USA	$8.9 \cdot 10^{-11}$ to $8.3 \cdot 10^{-10}$
Kaur et Anastasio 2017 [17]	Fog	California, USA	$2.3 \cdot 10^{-10}$ to $6.9 \cdot 10^{-10}$
Ma 2023 [18]	Particle extracts	California, USA	$2 \cdot 10^{-10}$ to $8.2 \cdot 10^{-8}$
Zhou 2008 [19]	Marine aerosols	Sargasso (Atlantic Ocean)	$1.1 \cdot 10^{-8}$ to $2.2 \cdot 10^{-7}$

7. Literature study of aerosol and cloud/fog concentrations of NO_3^-, H_2O_2, HULIS, and phenols/nitrophenols

In Table 1 in the main text, concentrations of the relevant species in aerosols and cloud/fog conditions are shown. These values originate from a literature study, in which concentrations of nitrate, hydrogen peroxide, and HULIS/(N)Ph concentrations were extracted from studies regarding measurements of aerosols or cloud/fog composition.

7.1 Method for "µg m^{-3} to mol L^{-1}" conversion

Here, a method for converting the concentrations of considered species from µg m^{-3} to mol L^{-1} is shown.

$$[comp]\left(\frac{mol}{L}\right) = \frac{\rho \cdot [comp] \cdot 10^{-9}}{[particles] \cdot M} \quad \text{(S4)}$$

Where ρ is the density of particles in units of $\mu g\ (particles)\ m^{-3}(particles)$, and is estimated to be 1.49 g cm^{-3} (average from eight articles reporting density of particles [20–27]). *[particles]* is the average concentration of particulate matter (unit: $\mu g\ (particles)\ m^{-3}(air)$) reported in correlation with the concentration of the given compound, *[comp]* (unit: $\mu g\ m^{-3}(air)$). *M* is the molar mass of the compound in units of $g\ mol^{-1}$.

7.2 Example of conversion

An example of the conversion of concentration is shown in the equation below.

Peng et al.[28] reports an annual nitrate concentration of 5.6 µg m^{-3} and an annual particle concentration of 56.2 µg m^{-3}. Here, the conversion into mol L^{-1} is shown.

$$\left[NO_3^-\right] = \frac{1.49 \cdot 10^{12} \mu g\ m^{-3} \cdot 5.6\ \mu g\ m^{-3} \cdot 10^{-9}}{56.2\ \mu g\ m^{-3} \cdot 62.0\ g\ mol^{-1}} = 2.39\ mol\ L^{-1}$$

7.3 Reported concentrations in literature

In the following tables, the result of the literature study is shown. The tables provide the references, the size and type of particles or cloud/fog, the location, the reported concentration of the species and particulate matter, as well as the species concentration converted into mol L^{-1}. This study was mainly focused on $PM_{2.5}$, though a few entries of other particle sizes were also included to have enough data.

7.3.1 Concentrations in aerosols

Table S4. Concentrations of nitrate anions in aerosols.

Reference	*Size/ type*	*Location*	*$[NO_3^-]$ ($\mu g\ m^{-3}$)*	*[PM] ($\mu g\ m^{-3}$)*	*$[NO_3^-]$ ($mol\ L^{-1}$)*
Bisht 2015 [29]	$PM_{2.5}$/ urban	Delhi, India	12.74	171.59	1.78
Christoforou, 2000 [30]	$PM_{2.5}$/ urban	California, USA	3.27	29.31	2.68
Christoforou, 2000 [30]	$PM_{2.5}$/ urban	California, USA	5.81	32.08	4.35
Christoforou, 2000 [30]	$PM_{2.5}$/ urban	California, USA	4.58	27.7	3.97
Kuang 2015 [31]	$PM_{2.5}$/ urban	Guangzhou, China	6.7	56	2.88
Lee 2020 [32]	$PM_{2.5}$/ urban	Seoul, South Korea	8.2	40.3	4.89
Li 2019 [33]	$PM_{2.5}$/ urban	Beijing, China	18.6	106	4.22
Shen 2009 [34]	PM_1 / urban	Xi'an, China	12.7	149.7	2.04
Tan 2017 [35]	$PM_{2.5}$/ urban	Lanzhou, China	7.21	120.5	1.44
Tan 2017 [35]	$PM_{2.5}$/ urban	Lanzhou, China	1.88	34.1	1.32
Wang 2019 [36]	$PM_{2.5}$/ urban – clean snowfall	Zhengzhou, China	18.9	49.7	9.14
Wang 2019 [36]	$PM_{2.5}$/ urban – polluted snowfall	Zhengzhou, China	39.1	121.6	7.73
Wang 2019 [36]	$PM_{2.5}$/ urban – clean haze	Zhengzhou, China	7.7	37.8	4.90
Wang 2019 [36]	$PM_{2.5}$/ urban – polluted haze	Zhengzhou, China	27.3	109	6.02

Wang 2019 [36]	$PM_{2.5}$/ urban – heavily polluted haze	Zhengzhou, China	75.3	267.4	6.77
Xu 2019 [37]	$PM_{2.5}$/ urban – clean haze	Beijing, China	6.64	32.21	4.95
Xu 2019 [37]	$PM_{2.5}$/ urban – moderately polluted haze	Beijing, China	22.95	91.84	6.00
Xu 2019 [37]	$PM_{2.5}$/ urban – heavily polluted haze	Beijing, China	44.52	167.51	6.39
Ye 2017 [38]	$PM_{2.5}$/ urban	Changzhou, China	19.3	108.3	4.28
Zhang 2018 [39]	$PM_{2.5}$/ urban – clear day	Beijing, China	4.81	17.9	6.46
Zhang 2018 [39]	$PM_{2.5}$/ urban – polluted	Beijing, China	26.03	142.8	4.38
Artaxo 2013 [40]	$PM_{2.5}$/ BB	Porto Velho, Brazil	0.22	33	0.16
Khamkaew 2016 [41]	$PM_{2.5}$/ BB	Chiang Mai, Thailand	4.13	82.1	1.21
Kumar 2018 [42]	PM_{10}/ urban - BB influenced	Kanpur, India	12.68	167	1.82
Kumar 2018 [42]	PM_{10}/ urban - BB influenced	Kanpur, India	29.24	283	2.48
Li 2014 [43]	$PM_{2.5}$/ BB (wheat straw)	Suixi, China	11.8	110.7	2.56
Pio 2008 [44]	$PM_{2.5}$/ BB	Pannonia, Hungary	0.401	38.1	0.25
Rastogi 2015 [45]	$PM_{2.5}$/ BB	Patiala, India	9.1	175	1.25
Rastogi 2015 [45]	$PM_{2.5}$/ BB	Patiala, India	21	169	2.99
Rastogi 2015 [45]	$PM_{2.5}$/ BB	Patiala, India	2.2	51	1.04
Rastogi 2015 [45]	$PM_{2.5}$/ BB	Patiala, India	1.5	82	0.44
Rastogi 2015 [45]	$PM_{2.5}$/ BB	Patiala, India	0.42	51	0.20
Ryu 2004 [46]	$PM_{2.5}$/ BB (barley)	Gwangju, South Korea	17.5	129.6	3.24

Ryu 2004 [46]	PM_{10}/ BB (barley)	Gwangju, South Korea	6.8	24.2	6.75
Peng 2019 [28]	$PM_{2.5}$/ rural background	JinYun, China	5.6	56.2	2.39
Rogula-Kozlowska and Klejnowski 2013 [47]	PM_1 / rural background	Raciborz, Poland	2.07	32.10	1.55
Alves 2007 [48]	PM_{16}/ coastal	Aveiro, Portugal	3.09	30.7	2.42
Song 2022 [49]	$PM_{2.5}$/ marine	South Korea	1.1	19.1	1.38
Xiao 2018 [50]	PM_1/ marine	Western North Pacific	1.2	44.8	0.64

Table S5. Concentrations of hydrogen peroxide in aerosols.

Reference	*Size/ type*	*Location*	*$[H_2O_2]$ (ng m^{-3})*	*[PM] (µg m^{-3})*	*$[H_2O_2]$ (mol L^{-1})*
Arellanes 2006 [51]	$PM_{2.5}$/ urban	California, USA	5.4	13	0.018
Arellanes 2006 [51]	$PM_{>2.5}$/ urban	California, USA	10	26	0.017
Wang 2010 [52]	$PM_{>2.5}$/ urban	California, USA	17	45.9	0.016
Xuan 2020 [53]	$PM_{2.5}$/ urban	Beijing, China	2.22	39.2	0.002

Table S6. Concentrations of HULIS in aerosols. [a]The values were reported in HULIS µg m^{-3} and was converted to µgC m^{-3} by a mass-to-carbon ratio of HULIS of 1.9, that the authors (Lin et al., 2010) estimated from literature.

Reference	*Size/ type*	*Location*	*[HULIS] (μgC m^{-3})*	*[PM] (μg m^{-3})*	*[HULIS] (mol L^{-1})*
Kuang 2015 [31]	$PM_{2.5}$/ urban	Guangzhou, China	4.8	56	10.6
Lee 2020 [32]	$PM_{2.5}$/ urban	Seoul, South Korea	2.0	40.3	6.16
Li 2019 [33]	$PM_{2.5}$/ urban	Beijing, China	3.95	107	4.58
Popovicheva 2020 [54]	PM_{10}/ urban background	Moscow, Russia	0.61	22	3.44
Tan 2017 [35]	$PM_{2.5}$/ urban	Lanzhou, China	4.02	121	4.14
Tan 2017 [35]	$PM_{2.5}$/ urban	Lanzhou, China	1.19	34.1	4.33
Ye 2017 [38]	$PM_{2.5}$/ urban	Changzhou, China	5.7	77.3	9.15
Zhang 2022 [25]	$PM_{2.5}$/ urban	Xi'an, China	11.6	179	8.03
Zhang 2022 [55]	$PM_{2.5}$/ urban	Xi'an, China	8.28	69.7	14.7
Kumar 2018 [42]	$PM_{2.5}$/ BB	Kanpur, India	12	167	8.91
Kumar 2018 [42]	$PM_{2.5}$/ BB	Kanpur, India	15.3	283	6.71
Lin 2010[a] [56]	$PM_{2.5}$/ rural BB (sugarcane)	Pearl River Delta region, China	116.3	2921	4.94
Lin 2010[a] [56]	$PM_{2.5}$/ rural BB (rice straw)	Pearl River Delta region, China	620	9537	8.07
Wang 2017 [57]	$PM_{2.5}$/ BB	Suixi, China	63.6	823	9.58
Kiss 2021 [58]	$PM_{2.5}$/ rural	Great Hungarian Plain, Hungary	1.54	22.9	8.34
Lin 2010[b] [56]	$PM_{2.5}$/ rural	Pearl River Delta region, China	6.21	105	7.34
Pio 2007 [59]	$PM_{2.5}$/ coastal	Aveiro, Portugal	1.92	23	10.4
Nguyen 2014 [60]	PM_{10}/ arctic	Greenland	$9 \cdot 10^{-3}$	1.0	1.12

7.3.2 Concentrations in cloud/fog

Table S7. Concentrations of nitrate anions in cloud/fog conditions. [a]average of 23 samples.

Reference	*Type*	*Location*	*$[NO_3^-]$ (mol L^{-1})*
Dui 2009 [61]	Fog/ urban	Guangzhou, China	$1.39 \cdot 10^{-2}$
Dui 2009 [61]	Fog/ urban	Southern Fujian, China	$2.57 \cdot 10^{-4}$
Fisak 2002 [62]	Cloud/ urban	Kopisty, Czech Republic	$1.61 \cdot 10^{-3}$
Fisak 2002 [62]	Cloud/ urban	Prague-Libus, Czech Republic	$7.74 \cdot 10^{-4}$
Fisak 2002 [62]	Cloud/ urban	Jablonec, Czech Republic	$1.31 \cdot 10^{-4}$
Giulianelli 2014 [63]	Fog/ urban	Po Valley, Italy	$1.13 \cdot 10^{-3}$
Munger 1989 [64]	Fog/ urban	California, USA	$8.42 \cdot 10^{-3}$
Bianco 2015 [15]	Cloud/ rural	Puy de Dôme, France	$3.69 \cdot 10^{-5}$
Charbouillot 2011 [1]	Cloud/ rural (continental)	Puy de Dôme, France	$4.68 \cdot 10^{-4}$
Charbouillot 2011 [1]	Cloud/ rural (marine)	Puy de Dôme, France	$3.48 \cdot 10^{-5}$
Cook 2017 [65]	Cloud/ rural (mountain)	New York, USA	$2.05 \cdot 10^{-5}$
Cook 2017 [65]	Cloud/ rural (mountain)	New York, USA	$1.16 \cdot 10^{-5}$
Cook 2017 [65]	Cloud/ rural (mountain)	New York, USA	$4.8 \cdot 10^{-6}$
Deguillaume 2014 [66]	Cloud/ rural (continental)	Puy de Dôme, France	$1.11 \cdot 10^{-4}$
Deguillaume 2014 [66]	Cloud/ rural (marine)	Puy de Dôme, France	$2.48 \cdot 10^{-5}$
Deguillaume 2014 [66]	Cloud/ rural (highly marine)	Puy de Dôme, France	$5.93 \cdot 10^{-5}$
Deguillaume 2014 [66]	Cloud/ rural (polluted)	Puy de Dôme, France	$4.17 \cdot 10^{-5}$
Marinoni 2011[a] [67]	Cloud/rural	Puy de Dôme, France	$8.94 \cdot 10^{-5}$
Beiderwieden 2005 [68]	Fog/ rural (mountain)	Loja, Ecuador	$4.01 \cdot 10^{-5}$
Corell 2010 [69]	Fog/ rural (mountain)	Valencia, Spain	$1.03 \cdot 10^{-3}$

Corell 2021 [70]	Fog/ rural (mountain)	Mt. Monduver, Spain	$2.10 \cdot 10^{-4}$
Fisak 2002 [62]	Cloud/ rural (mountain)	Milesovka, Czech	$5.31 \cdot 10^{-4}$
Fisak 2002 [62]	Cloud/ rural (mountain)	Churanov, Czech	$3.47 \cdot 10^{-4}$
Li 2017 [71]	Cloud/ rural (mountain)	Mt. Tai, China	$9.10 \cdot 10^{-4}$
Vega 2019 [72]	Cloud/ rural (mountain)	Mt. Areskutan, Sweden	$3.5 \cdot 10^{-5}$
Wrzesinsky and Klemm 2000 [73]	Fog/ rural (mountain)	Fichtelbirge mountains, Germany	$4.81 \cdot 10^{-4}$
Watanabe and Ishizaka 1999 [74]	Fog/ rural (mountain)	Mt. Norikura, Japan	$2.25 \cdot 10^{-4}$
Wu 2009 [61]	Fog/ rural (mountain)	Lushan mt., China	$7.3 \cdot 10^{-5}$
Wu 2009 [61]	Fog/ rural (mountain)	Nan Ling Mts., China	$9.7 \cdot 10^{-5}$

Table S8. Concentrations of hydrogen peroxide in cloud/fog conditions. [a]average of 23 samples

Reference	*Type*	*Location*	*$[H_2O_2]$ (mol L^{-1})*
Munger 1989 [64]	Fog/ urban	California, USA	$1.47 \cdot 10^{-5}$
Xuan 2020 [53]	Cloud/ urban	Beijing, China	$4.82 \cdot 10^{-5}$
Bianco 2015 [15]	Cloud/ rural	Puy de Dôme, France	$1.21 \cdot 10^{-5}$
Claiborn and Aneja 1991 [75]	Cloud/ rural (mountain)	North Carolina, USA	$3.80 \cdot 10^{-5}$
Claiborn and Aneja 1991 [75]	Cloud/ rural (mountain)	North Carolina, USA	$4.40 \cdot 10^{-5}$
Charbouillot 2011 [1]	Cloud/ rural (marine)	Puy de Dôme, France	$3.90 \cdot 10^{-6}$
Charbouillot 2011 [1]	Cloud/ rural (continental)	Puy de Dôme, France	$1.98 \cdot 10^{-5}$

Deguillaume 2014 [66]	Cloud/ rural (polluted)	Puy de Dôme, France	$4.90 \cdot 10^{-6}$
Deguillaume 2014 [66]	Cloud/ rural (continental)	Puy de Dôme, France	$9.90 \cdot 10^{-6}$
Deguillaume 2014 [66]	Cloud/ rural (marine)	Puy de Dôme, France	$6.20 \cdot 10^{-6}$
Deguillaume 2014 [66]	Cloud/ rural (highly marine)	Puy de Dôme, France	$1.12 \cdot 10^{-5}$
Li 2017 [71]	Cloud/ rural (mountain)	Mt. Tai, China	$2.35 \cdot 10^{-5}$
Marinoni 2011[a] [67]	Cloud/ rural	Puy de Dôme, France	$7.22 \cdot 10^{-6}$
van Pinxteren 2016 [76]	Cloud/ rural (mountain)	Mt. Schmücke, Germany	$5.60 \cdot 10^{-6}$
Watanabe and Ishizaka 1999 [74]	Cloud/ rural (mountain)	Mt. Norikura, Japan	$6.00 \cdot 10^{-5}$
Benedict 2012 [77]	Cloud/ marine	Pacific Ocean	$1.20 \cdot 10^{-4}$
Straub 2007 [78]	Cloud/ marine	Pacific Ocean	$1.14 \cdot 10^{-4}$

Table S9. Concentrations of phenols and nitrophenols in cloud/fog conditions.

Reference	*Compound*	*Type*	*Location*	*[(N)Ph] (mol L^{-1})*
Hofmann and Hartmann 2008 [79]	4-nitrophenol	Fog/ rural (mountain)	Waldstein, Germany	$6.69 \cdot 10^{-8}$
Hofmann and Hartmann 2008 [79]	2,4-dinitrophenol	Fog/ rural (mountain)	Waldstein, Germany	$1.17 \cdot 10^{-8}$
Richartz 1990 [80]	4-nitrophenol	Fog/ rural (mountain)	Fichtelbirge mountains, Germany	$1.45 \cdot 10^{-7}$
Richartz 1990 [80]	2,4-dinitrophenol	Fog/ rural (mountain)	Fichtelbirge mountains,	$7.10 \cdot 10^{-8}$

			Germany	
Richartz 1990 [80]	Phenol	Fog/ rural (mountain)	Fichtelbirge mountains, Germany	$6.99 \cdot 10^{-8}$
Richartz 1990 [80]	Dinitroorthocresol	Fog/ rural (mountain)	Fichtelbirge mountains, Germany	$2.01 \cdot 10^{-8}$
Richartz 1990 [80]	3-methyl-4-nitrophenol	Fog/ rural (mountain)	Fichtelbirge mountains, Germany	$2.41 \cdot 10^{-8}$
Boris 2016 [81]	4-nitrophenol	Fog/ costal	Baengnyeong Island, South Korea	$9.50 \cdot 10^{-8}$
Boris 2016 [81]	2,4-dinitrophenol	Fog/ costal	Baengnyeong Island, South Korea	$4.85 \cdot 10^{-8}$
Boris 2018 [82]	4-nitrophenol	Fog/ costal	California, USA	$6.92 \cdot 10^{-9}$
Boris 2018 [82]	2,4-dinitrophenol	Fog/ costal	California, USA	$1.13 \cdot 10^{-8}$
Boris 2018 [82]	3-methyl-4-nitrophenol	Fog/ costal	California, USA	$7.93 \cdot 10^{-9}$
Sagebiel and Seiber 1993 [83]	Syringol	Fog/ urban	California, USA	$1.53 \cdot 10^{-6}$
Sagebiel and Seiber 1993 [83]	Creosol	Fog/ urban	California, USA	$3.67 \cdot 10^{-7}$
Sagebiel and Seiber 1993 [83]	Eugenol	Fog/ urban	California, USA	$1.86 \cdot 10^{-7}$
Sagebiel and Seiber 1993 [83]	Vanillin	Fog/ urban	California, USA	$4.50 \cdot 10^{-7}$
Sagebiel and Seiber 1993 [83]	Isoeugenol	Fog/ urban	California, USA	$1.89 \cdot 10^{-7}$
Sagebiel and Seiber 1993 [83]	4-acetylguaiacol	Fog/ urban	California, USA	$3.21 \cdot 10^{-8}$
Sagebiel and	4-formylsyringol	Fog/ urban	California,	$1.76 \cdot 10^{-7}$

Seiber 1993 [83]				USA	
Hofmann and Hartmann 2008 [79]	4-nitrophenol	Cloud/ rural		Holme Moss, UK	$2.19 \cdot 10^{-7}$
Hofmann and Hartmann 2008 [79]	2,4-dinitrophenol	Cloud/ rural		Holme Moss, UK	$4.50 \cdot 10^{-8}$
Lallement 2018 [84]	Phenol	Cloud/ (mountain)	rural	Puy de Dôme, France	$4.99 \cdot 10^{-9}$
Lebedev 2018 [85]	4-nitrophenol	Cloud/ (mountain)	rural	Puy de Dôme, France	$3.59 \cdot 10^{-10}$
Lebedev 2018 [85]	Phenol	Cloud/ (mountain)	rural	Puy de Dôme, France	$7.08 \cdot 10^{-9}$
Lebedev 2018 [85]	Cresol	Cloud/ (mountain)	rural	Puy de Dôme, France	$1.85 \cdot 10^{-9}$
Lebedev 2018 [85]	4-ethylphenol	Cloud/ (mountain)	rural	Puy de Dôme, France	$4.07 \cdot 10^{-9}$
Lebedev 2018 [85]	3,4-dimethylphenol	Cloud/ (mountain)	rural	Puy de Dôme, France	$2.70 \cdot 10^{-9}$
Levsen 1993 [86]	4-nitrophenol	Cloud/ (mountain)	rural	Vosges, France	$3.93 \cdot 10^{-8}$
Levsen 1993 [86]	Phenol	Cloud/ (mountain)	rural	Vosges, France	$3.67 \cdot 10^{-8}$
Levsen 1993 [86]	Cresol	Cloud/ (mountain)	rural	Vosges, France	$1.02 \cdot 10^{-8}$
Lüttke 1997 [87]	4-nitrophenol	Cloud/ (mountain)	rural	Great Dun Fell, England	$1.55 \cdot 10^{-8}$
Lüttke 1999 [88]	4-nitrophenol	Cloud/ (mountain)	rural	Mount Brocken, Germany	$1.51 \cdot 10^{-7}$
Lüttke 1997 [87]	2,4-dinitrophenol	Cloud/ (mountain)	rural	Great Dun Fell, England	$5.67 \cdot 10^{-9}$
Lüttke 1999 [88]	2,4-dinitrophenol	Cloud/ (mountain)	rural	Mount Brocken, Germany	$2.93 \cdot 10^{-8}$

Lüttke 1997 [87]	Phenol	Cloud/ (mountain)	rural	Great Dun Fell, England	$5.74 \cdot 10^{-8}$
Lüttke 1999 [88]	Phenol	Cloud/ (mountain)	rural	Mount Brocken, Germany	$3.19 \cdot 10^{-8}$
Lüttke 1999 [88]	2-methylphenol	Cloud/ (mountain)	rural	Mount Brocken, Germany	$2.77 \cdot 10^{-9}$
Lüttke 1997 [87]	2-nitrophenol	Cloud/ (mountain)	rural	Great Dun Fell, England	$1.63 \cdot 10^{-9}$
Lüttke 1999 [88]	2- nitrophenol	Cloud/ (mountain)	rural	Mount Brocken, Germany	$2.16 \cdot 10^{-9}$
Lüttke 1997 [87]	Dinitroorthocresol	Cloud/ (mountain)	rural	Great Dun Fell, England	$3.65 \cdot 10^{-9}$
Lüttke 1999 [88]	Dinitroorthocresol	Cloud/ (mountain)	rural	Mount Brocken, Germany	$2.12 \cdot 10^{-8}$
Lüttke 1999 [88]	Cresol	Cloud/ (mountain)	rural	Mount Brocken, Germany	$1.57 \cdot 10^{-8}$

8. Additional figures

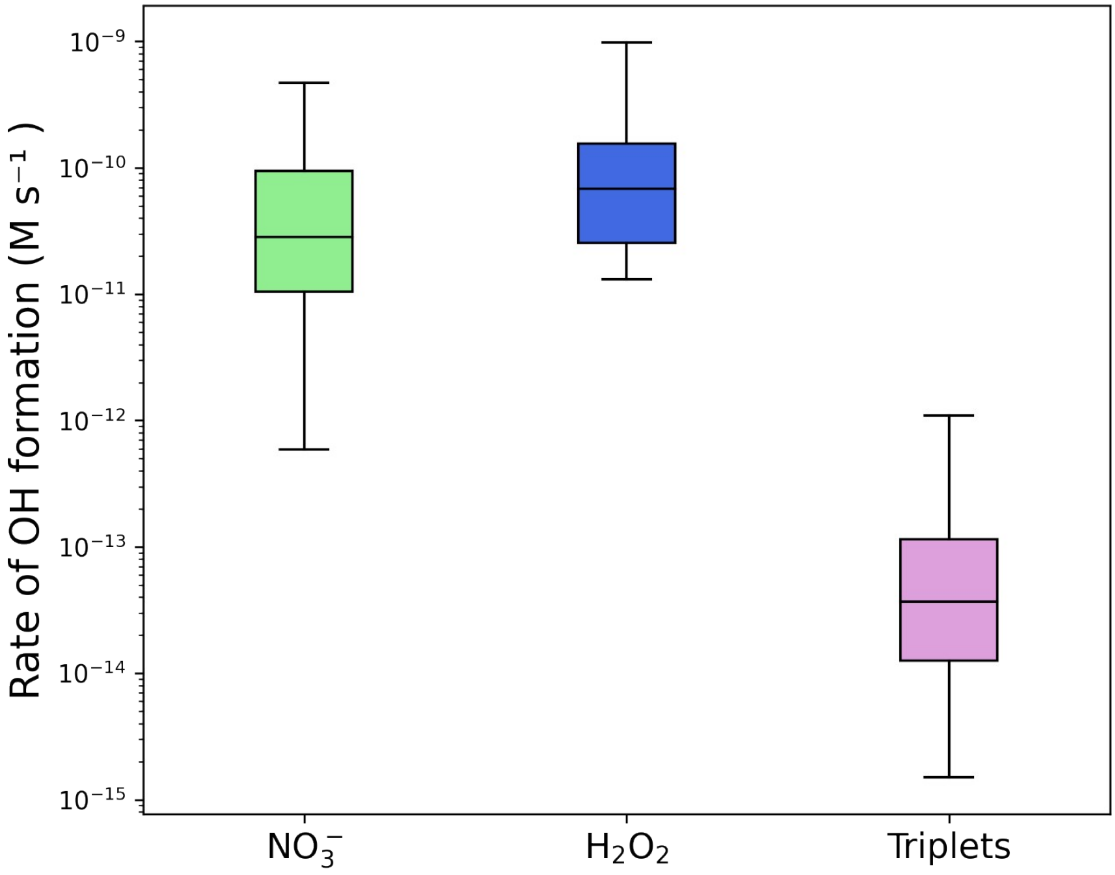

Figure S13. Boxplot OH of formation rates in rural clouds using (N)Ph concentrations for triplet state approximations.

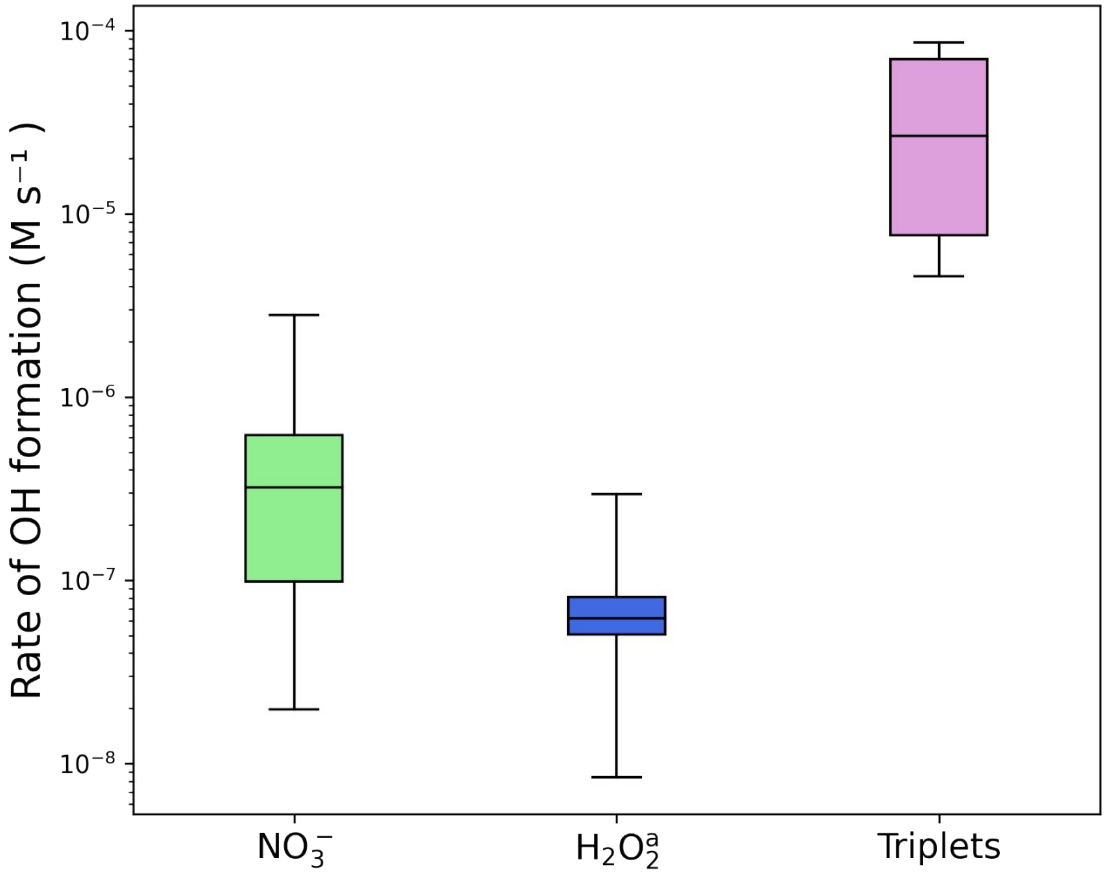

Figure S14. Boxplot of OH formation rates in biomass burning aerosols HULIS concentrations were used for triplet state approximations. [a]It was not possible to find H_2O_2 concentrations in biomass burning aerosols, and therefore an average of all urban concentrations was applied.

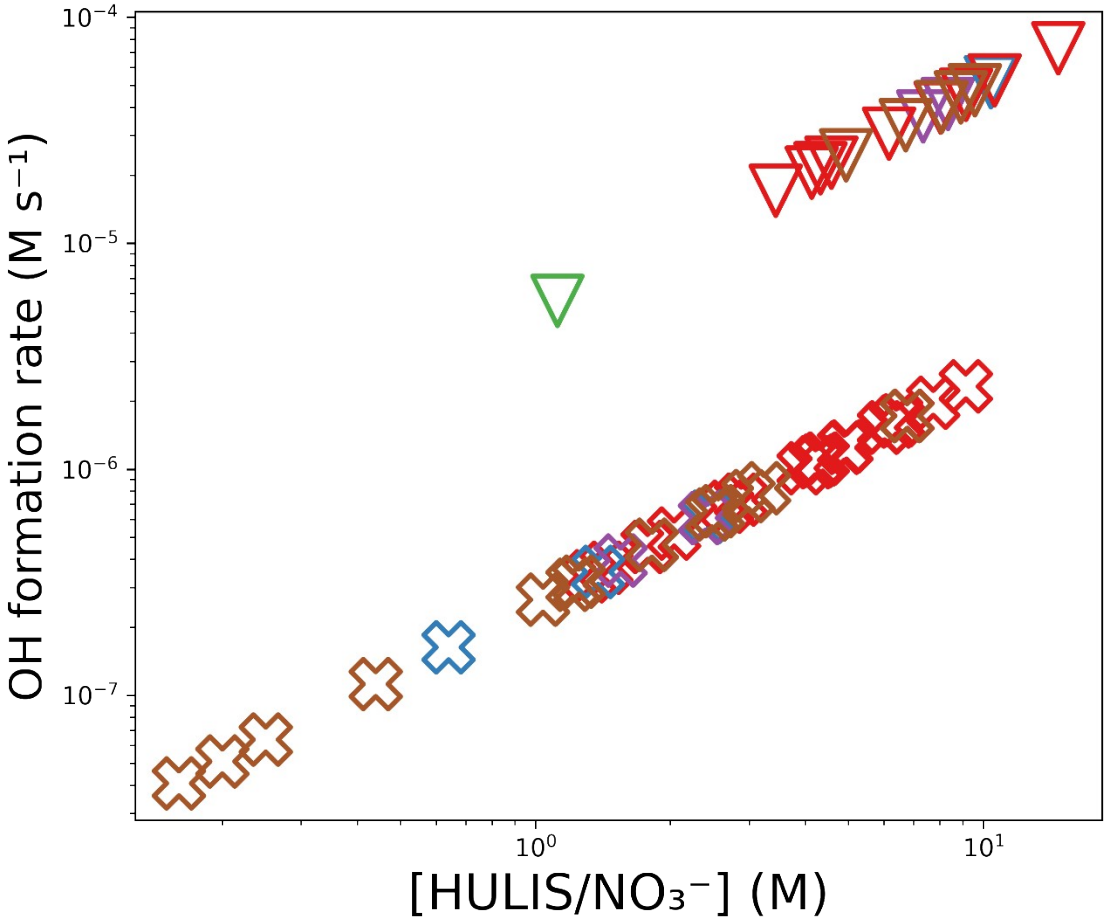

Figure S15. Zoom of the aerosol HULIS/NO_3^- region of Figure 4 in the main text.

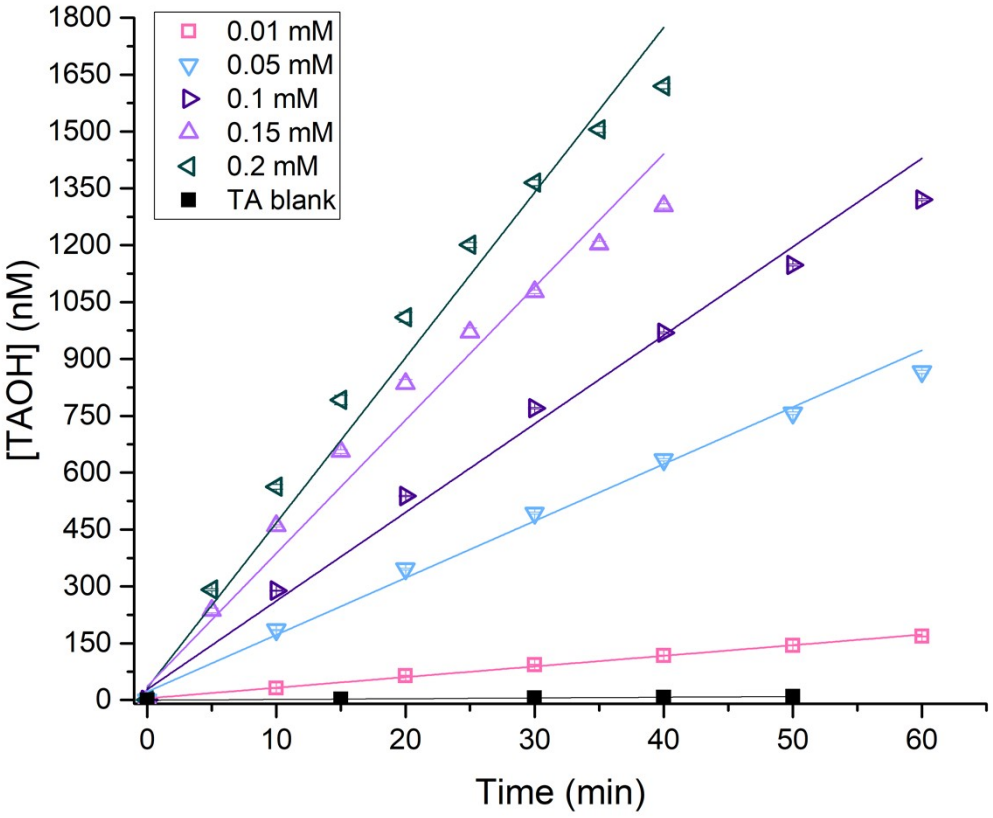

Figure S16. TAOH formation from H_2O_2 at various concentrations.

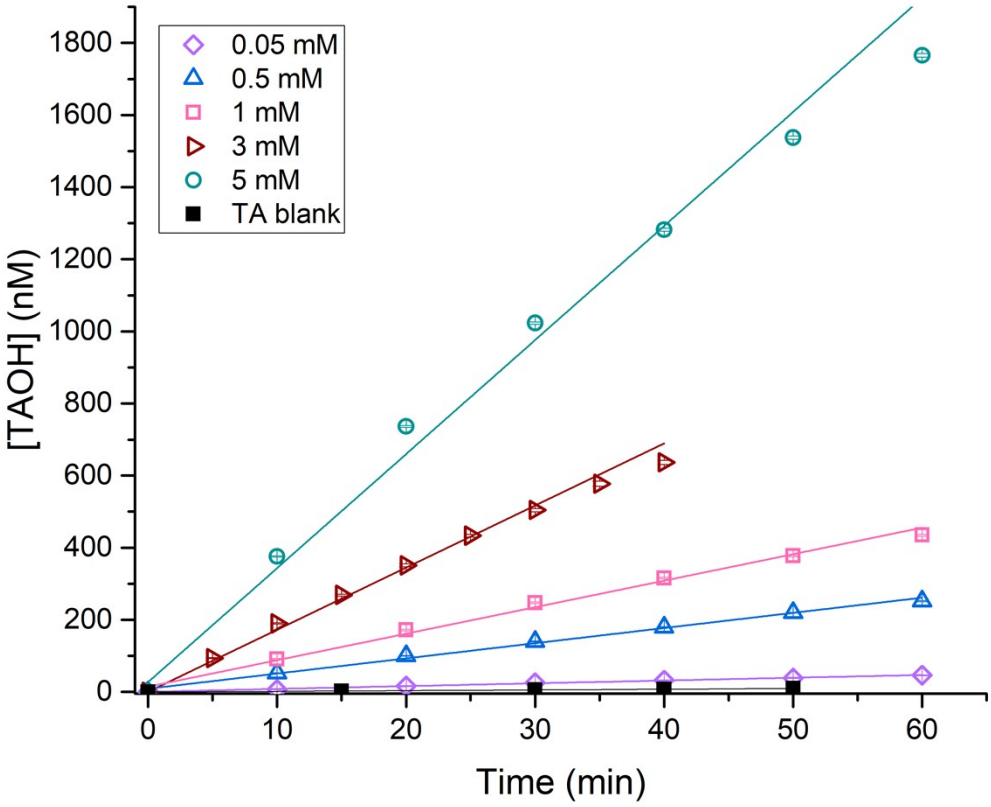

Figure S17. TAOH formation from NO_3^- with various concentrations.

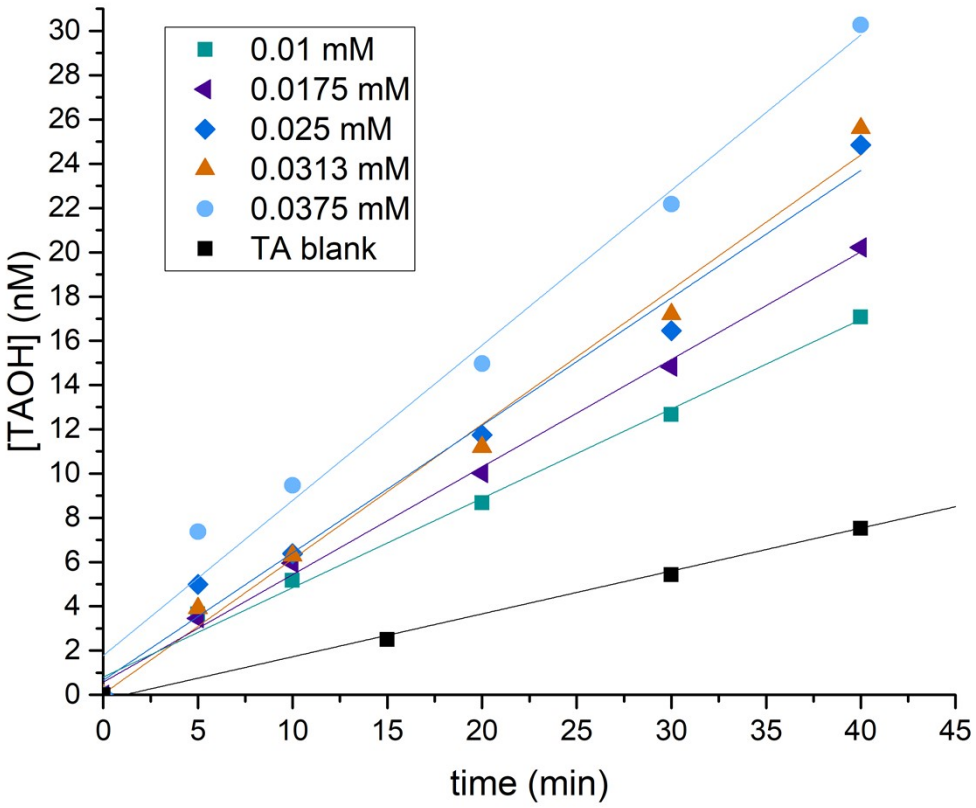

Figure S18. TAOH formation from 4HB with various concentrations.

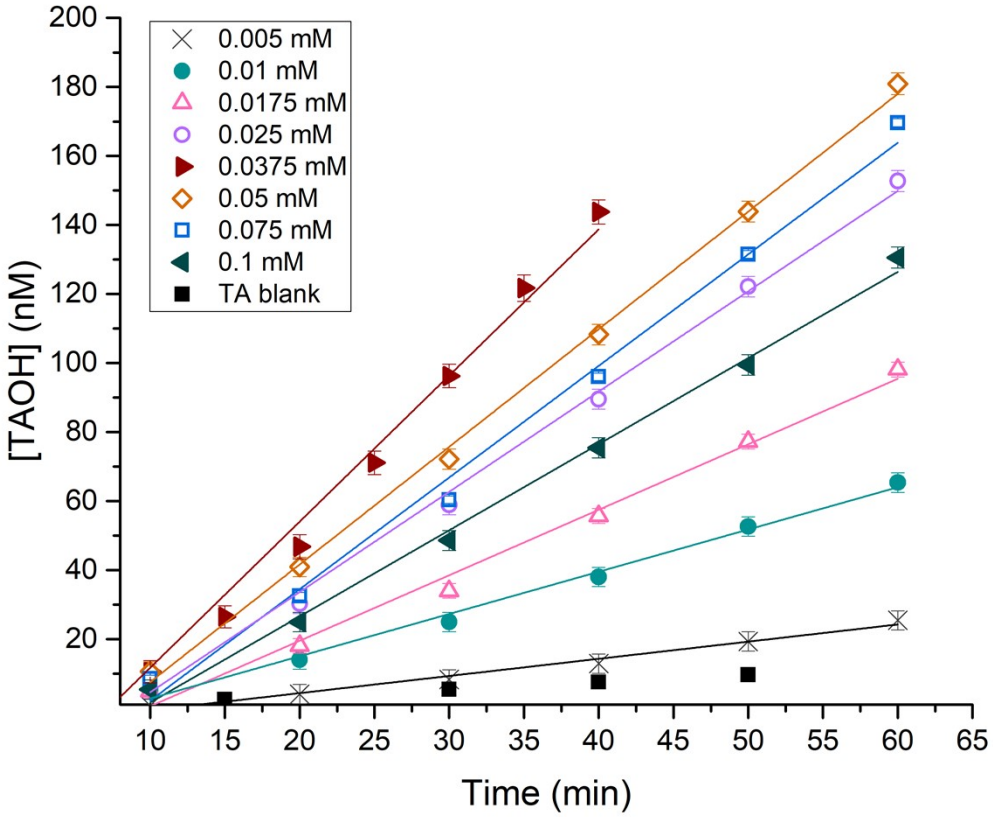

Figure S19. The TAOH formation from various concentrations of VL, and from a TA control experiment.

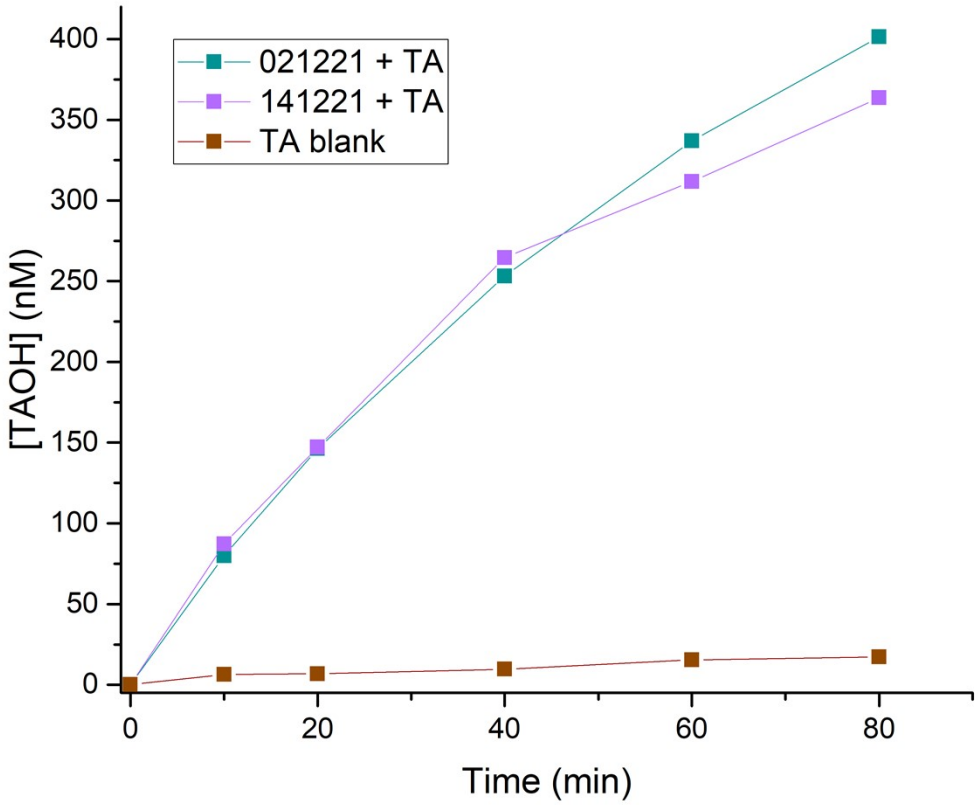

Figure S20. TAOH formation from the two aerosol samples (021221 and 141221), as well as a blank TA experiment. All three experiments had a TA concentration of 500 μM.

9. Decay of triplet state source

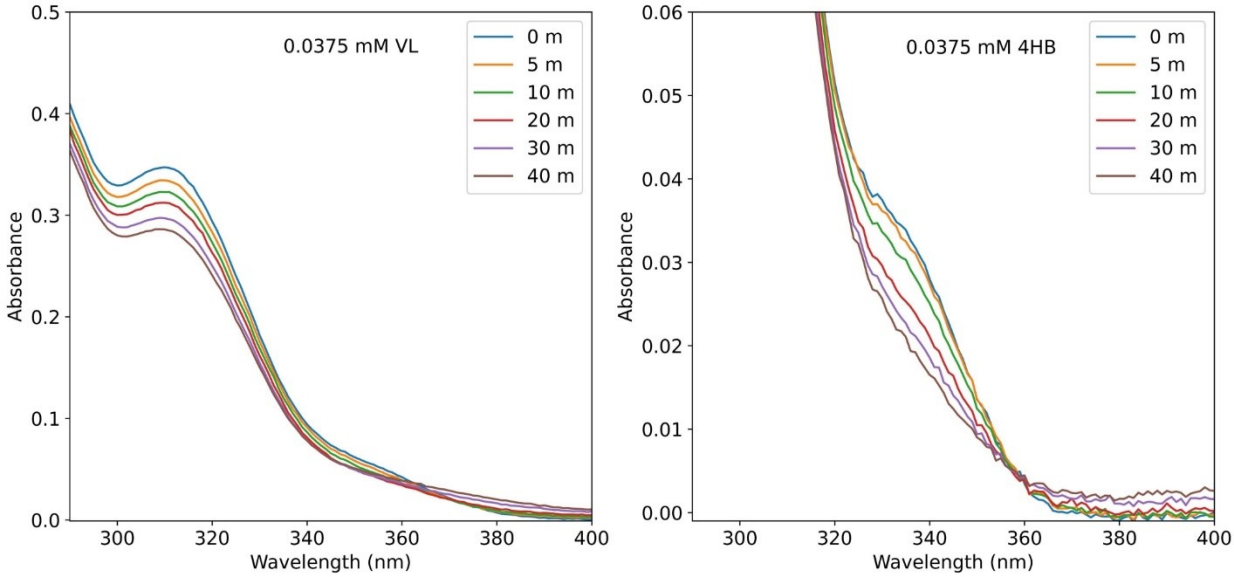

Figure S21. UV-Vis spectra that show the decay of VL (left) and 4HB (right) during the experiments with concentrations of 0.037 mM. Both had approximately linear decays with first-order rate constants of 7.59×10^{-5} s^{-1} and 1.80×10^{-4} s^{-1} for VL and 4HB, respectively.

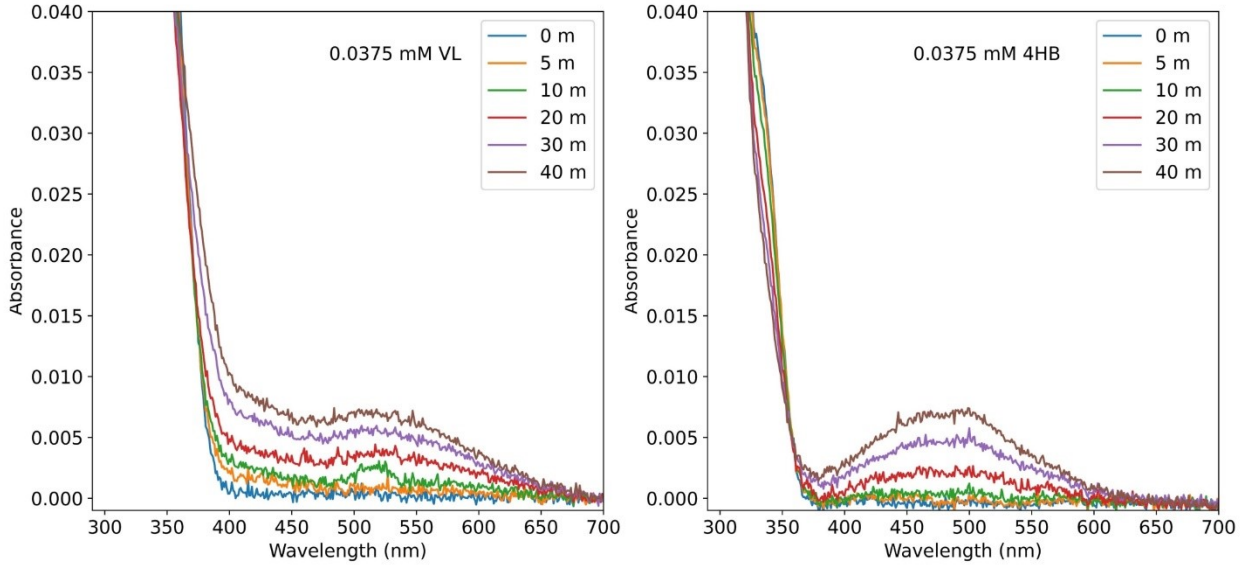

Figure S22. UV-vis spectra showing the formation of light absorbing species in the visible range from both the VL (left) and 4HB (right) experiments with concentrations of 0.037 mM.

10. Quantum yields of OH formation

Quantum yields were calculated as previously proposed by Bianco et al. [15], according to Equation (S5).

$$\Phi_{280-600nm} = \frac{R_{OH}}{R_{abs}} \quad \text{(S5)}$$

Here R_{OH} is the rate of OH formation from the compounds, and R_{abs} is the rate of light absorption by the solution and is calculated by the following (Equation S6) [89],

$$R_{abs} = 2.303 \times 10^3 \times \Sigma(\alpha_\lambda \times I_\lambda \times \Delta\lambda) \quad \text{(S6)}$$

where α_λ is the absorbance of the sample at the given wavelength (cm^{-1}), I_λ is the irradiance of the lamp at the given wavelength ($mol_{photons}\ s^{-1}\ cm^{-2}\ nm^{-1}$), and $\Delta\lambda$ is the wavelength interval (nm). 2.3 is used for base conversion, and 10^3 is applied for unit conversion.

The screening factors are calculated by [90],

$$sf = \frac{\Sigma(1 - 10^{-(l \times \alpha_\lambda)} \times I_\lambda)}{\Sigma(2.303 \times l \times \alpha_\lambda \times I_\lambda)} \quad \text{(S7)}$$

where l is the path length of the light through the sample.

Table S10. Quantum yields, rate of light absorption, and screening factors for VL and 4HB ($[VL]_0$ = 37 µM, $[4HB]_0$ = 37 µM,) at the beginning (t = 0 min) and end (t = 40 min) of the experiments and from the aerosol samples 021221 and 141221 (t = 0 min). Values from VL and 4HB are from duplicate experiments. The errors are from one standard deviation.

	$\Phi_{(280\text{-}600nm)}$	R_{abs} ($mol_{photons}\ L^{-1}\ s^{-1}$)	*screening factor*
VL (t = 0 min)	$(1.04 \pm 0.020) \times 10^{-4}$	$(2.27 \pm 0.097) \times 10^{-6}$	0.80 ± 0.003
4HB (t = 0 min)	$(1.12 \pm 0.29) \times 10^{-4}$	$(6.89 \pm 1.53) \times 10^{-7}$	0.77 ± 0.05
Sample 02122021	3.26×10^{-5}	2.98×10^{-6}	0.75
Sample 14122021	4.39×10^{-5}	1.87×10^{-6}	0.81

References

(1) Charbouillot, T.; Brigante, M.; Mailhot, G.; Maddigapu, P. R.; Minero, C.; Vione, D. Performance and Selectivity of the Terephthalic Acid Probe for OH as a Function of Temperature, PH and Composition of Atmospherically Relevant Aqueous Media. *Journal of Photochemistry and Photobiology A: Chemistry* **2011**, *222* (1), 70–76. https://doi.org/10.1016/j.jphotochem.2011.05.003.

(2) Leyssens, G.; Louis, F.; Sawerysyn, J.-P. Temperature Dependence of the Mass Accommodation Coefficients of 2-Nitrophenol, 2-Methylphenol, 3-Methylphenol, and 4-Methylphenol on Aqueous Surfaces. *J. Phys. Chem. A* **2005**, *109* (9), 1864–1872. https://doi.org/10.1021/jp0474430.

(3) Wenk, J.; Eustis, S. N.; McNeill, K.; Canonica, S. Quenching of Excited Triplet States by Dissolved Natural Organic Matter. *Environ. Sci. Technol.* **2013**, *47* (22), 12802–12810. https://doi.org/10.1021/es402668h.

(4) Canonica, S.; Hellrung, B.; Wirz, J. Oxidation of Phenols by Triplet Aromatic Ketones in Aqueous Solution. *J. Phys. Chem. A* **2000**, *104* (6), 1226–1232. https://doi.org/10.1021/jp9930550.

(5) McCabe, A. J.; Arnold, W. A. Reactivity of Triplet Excited States of Dissolved Natural Organic Matter in Stormflow from Mixed-Use Watersheds. *Environ. Sci. Technol.* **2017**, *51* (17), 9718–9728. https://doi.org/10.1021/acs.est.7b01914.

(6) al Housari, F.; Vione, D.; Chiron, S.; Barbati, S. Reactive Photoinduced Species in Estuarine Waters. Characterization of Hydroxyl Radical, Singlet Oxygen and Dissolved Organic Matter Triplet State in Natural Oxidation Processes. *Photochem Photobiol Sci* **2010**, *9* (1), 78–86. https://doi.org/10.1039/b9pp00030e.

(7) Erickson, P. R.; Moor, K. J.; Werner, J. J.; Latch, D. E.; Arnold, W. A.; McNeill, K. Singlet Oxygen Phosphorescence as a Probe for Triplet-State Dissolved Organic Matter Reactivity. *Environ. Sci. Technol.* **2018**, *52* (16), 9170–9178. https://doi.org/10.1021/acs.est.8b02379.

(8) Moor, K. J.; Schmitt, M.; Erickson, P. R.; McNeill, K. Sorbic Acid as a Triplet Probe: Triplet Energy and Reactivity with Triplet-State Dissolved Organic Matter via 1O2 Phosphorescence. *Environ. Sci. Technol.* **2019**, *53* (14), 8078–8086. https://doi.org/10.1021/acs.est.9b01787.

(9) Lallement, A.; Vinatier, V.; Brigante, M.; Deguillaume, L.; Delort, A. M.; Mailhot, G. First Evaluation of the Effect of Microorganisms on Steady State Hydroxyl Radical Concentrations in Atmospheric Waters. *Chemosphere* **2018**, *212*, 715–722. https://doi.org/10.1016/j.chemosphere.2018.08.128.

(10) Anastasio, C.; Jordan, A. L. Photoformation of Hydroxyl Radical and Hydrogen Peroxide in Aerosol Particles from Alert, Nunavut: Implications for Aerosol and Snowpack Chemistry in the Arctic. *Atmospheric Environment* **2004**, *38* (8), 1153–1166. https://doi.org/10.1016/j.atmosenv.2003.11.016.

(11) Anastasio, C.; McGregor, K. G. Chemistry of Fog Waters in California's Central Valley: 1. In Situ Photoformation of Hydroxyl Radical and Singlet Molecular Oxygen. *Atmospheric Environment* **2001**, *35* (6), 1079–1089. https://doi.org/10.1016/S1352-2310(00)00281-8.

(12) Anastasio, C.; Newberg, J. T. Sources and Sinks of Hydroxyl Radical in Sea-Salt Particles. *Journal of Geophysical Research: Atmospheres* **2007**, *112* (D10). https://doi.org/10.1029/2006JD008061.

(13) Arakaki, T.; Kuroki, Y.; Okada, K.; Nakama, Y.; Ikota, H.; Kinjo, M.; Higuchi, T.; Uehara, M.; Tanahara, A. Chemical Composition and Photochemical Formation of Hydroxyl Radicals in Aqueous Extracts of Aerosol Particles Collected in Okinawa, Japan. *Atmospheric Environment* **2006**, *40* (25), 4764–4774. https://doi.org/10.1016/j.atmosenv.2006.04.035.
(14) Arakaki, T.; Faust, B. C. Sources, Sinks, and Mechanisms of Hydroxyl Radical (•OH) Photoproduction and Consumption in Authentic Acidic Continental Cloud Waters from Whiteface Mountain, New York: The Role of the Fe(r) (r = II, III) Photochemical Cycle. *Journal of Geophysical Research: Atmospheres* **1998**, *103* (D3), 3487–3504. https://doi.org/10.1029/97JD02795.
(15) Bianco, A.; Passananti, M.; Perroux, H.; Voyard, G.; Mouchel-Vallon, C.; Chaumerliac, N.; Mailhot, G.; Deguillaume, L.; Brigante, M. A Better Understanding of Hydroxyl Radical Photochemical Sources in Cloud Waters Collected at the Puy de Dôme Station – Experimental versus Modelled Formation Rates. *Atmospheric Chemistry and Physics* **2015**, *15* (16), 9191–9202. https://doi.org/10.5194/acp-15-9191-2015.
(16) Faust, B. C.; Allen, J. M. Aqueous-Phase Photochemical Formation of Hydroxyl Radical in Authentic Cloudwaters and Fogwaters. *Environ. Sci. Technol.* **1993**, *27* (6), 1221–1224. https://doi.org/10.1021/es00043a024.
(17) Kaur, R.; Anastasio, C. Light Absorption and the Photoformation of Hydroxyl Radical and Singlet Oxygen in Fog Waters. *Atmospheric Environment* **2017**, *164*, 387–397. https://doi.org/10.1016/j.atmosenv.2017.06.006.
(18) Ma, L.; Worland, R.; Jiang, W.; Niedek, C.; Guzman, C.; Bein, K. J.; Zhang, Q.; Anastasio, C. Predicting Photooxidant Concentrations in Aerosol Liquid Water Based on Laboratory Extracts of Ambient Particles. *Atmos. Chem. Phys.* **2023**, *23* (15), 8805–8821. https://doi.org/10.5194/acp-23-8805-2023.
(19) Zhou, X.; Davis, A. J.; Kieber, D. J.; Keene, W. C.; Maben, J. R.; Maring, H.; Dahl, E. E.; Izaguirre, M. A.; Sander, R.; Smoydzyn, L. Photochemical Production of Hydroxyl Radical and Hydroperoxides in Water Extracts of Nascent Marine Aerosols Produced by Bursting Bubbles from Sargasso Seawater. *Geophysical Research Letters* **2008**, *35* (20). https://doi.org/10.1029/2008GL035418.
(20) Qiao, K.; Wu, Z.; Pei, X.; Liu, Q.; Shang, D.; Zheng, J.; Du, Z.; Zhu, W.; Wu, Y.; Lou, S.; Guo, S.; Chan, C. K.; Pathak, R. K.; Hallquist, M.; Hu, M. Size-Resolved Effective Density of Submicron Particles during Summertime in the Rural Atmosphere of Beijing, China. *Journal of Environmental Sciences* **2018**, *73*, 69–77. https://doi.org/10.1016/j.jes.2018.01.012.
(21) Kannosto, J.; Virtanen, A.; Lemmetty, M.; Mäkelä, J. M.; Keskinen, J.; Junninen, H.; Hussein, T.; Aalto, P.; Kulmala, M. Mode Resolved Density of Atmospheric Aerosol Particles. *Atmospheric Chemistry and Physics* **2008**, *8* (17), 5327–5337. https://doi.org/10.5194/acp-8-5327-2008.
(22) Pitz, M.; Cyrys, J.; Karg, E.; Wiedensohler, A.; Wichmann, H.-E.; Heinrich, J. Variability of Apparent Particle Density of an Urban Aerosol. *Environ. Sci. Technol.* **2003**, *37* (19), 4336–4342. https://doi.org/10.1021/es034322p.
(23) Geller, M.; Biswas, S.; Sioutas, C. Determination of Particle Effective Density in Urban Environments with a Differential Mobility Analyzer and Aerosol Particle Mass Analyzer. *Aerosol Science and Technology* **2006**, *40* (9), 709–723. https://doi.org/10.1080/02786820600803925.

(24) McMurry, P. H.; Wang, X.; Park, K.; Ehara, K. The Relationship between Mass and Mobility for Atmospheric Particles: A New Technique for Measuring Particle Density. *Aerosol Science and Technology* **2002**, *36* (2), 227–238. https://doi.org/10.1080/027868202753504083.
(25) Zhou, Y.; Ma, N.; Wang, Q.; Wang, Z.; Chen, C.; Tao, J.; Hong, J.; Peng, L.; He, Y.; Xie, L.; Zhu, S.; Zhang, Y.; Li, G.; Xu, W.; Cheng, P.; Kuhn, U.; Zhou, G.; Fu, P.; Zhang, Q.; Su, H.; Cheng, Y. Bimodal Distribution of Size-Resolved Particle Effective Density: Results from a Short Campaign in a Rural Environment over the North China Plain. *Atmospheric Chemistry and Physics* **2022**, *22* (3), 2029–2047. https://doi.org/10.5194/acp-22-2029-2022.
(26) Pokorná, P.; Zíková, N.; Vodička, P.; Lhotka, R.; Mbengue, S.; Holubová Šmejkalová, A.; Riffault, V.; Ondráček, J.; Schwarz, J.; Ždímal, V. Chemically Speciated Mass Size Distribution, Particle Density, Shape and Origin of Non-Refractory PM_1 Measured at a Rural Background Site in Central Europe. *Atmospheric Chemistry and Physics* **2022**, *22* (9), 5829–5858. https://doi.org/10.5194/acp-22-5829-2022.
(27) Hu, M.; Peng, J.; Sun, K.; Yue, D.; Guo, S.; Wiedensohler, A.; Wu, Z. Estimation of Size-Resolved Ambient Particle Density Based on the Measurement of Aerosol Number, Mass, and Chemical Size Distributions in the Winter in Beijing. *Environ. Sci. Technol.* **2012**, *46* (18), 9941–9947. https://doi.org/10.1021/es204073t.
(28) Peng, C.; Tian, M.; Chen, Y.; Wang, H.; Zhang, L.; Shi, G.; Liu, Y.; Yang, F.; Zhai, C. Characteristics, Formation Mechanisms and Potential Transport Pathways of PM2.5 at a Rural Background Site in Chongqing, Southwest China. *Aerosol Air Qual. Res.* **2019**, *19* (9), 1980–1992. https://doi.org/10.4209/aaqr.2019.01.0010.
(29) Bisht, D. S.; Dumka, U. C.; Kaskaoutis, D. G.; Pipal, A. S.; Srivastava, A. K.; Soni, V. K.; Attri, S. D.; Sateesh, M.; Tiwari, S. Carbonaceous Aerosols and Pollutants over Delhi Urban Environment: Temporal Evolution, Source Apportionment and Radiative Forcing. *Science of The Total Environment* **2015**, *521–522*, 431–445. https://doi.org/10.1016/j.scitotenv.2015.03.083.
(30) Christoforou, C. S.; Salmon, L. G.; Hannigan, M. P.; Solomon, P. A.; Cass, G. R. Trends in Fine Particle Concentration and Chemical Composition in Southern California. *Journal of the Air & Waste Management Association* **2000**, *50* (1), 43–53. https://doi.org/10.1080/10473289.2000.10463985.
(31) Kuang, B. Y.; Lin, P.; Huang, X. H. H.; Yu, J. Z. Sources of Humic-like Substances in the Pearl River Delta, China: Positive Matrix Factorization Analysis of $PM^{2.5}$ Major Components and Source Markers. *Atmospheric Chemistry and Physics* **2015**, *15* (4), 1995–2008. https://doi.org/10.5194/acp-15-1995-2015.
(32) Lee, H.-M.; Lee, S. P.; Li, Y.; Yu, J. Z.; Kim, J. Y.; Kim, Y. P.; Lee, J. Y. Characterization of Seasonal Difference of HULIS-C Sources from Water Soluble PM2.5 in Seoul, Korea: Probing Secondary Processes. *Aerosol Air Qual. Res.* **2020**, *21* (2), 200233. https://doi.org/10.4209/aaqr.2020.05.0233.
(33) Li, X.; Han, J.; Hopke, P. K.; Hu, J.; Shu, Q.; Chang, Q.; Ying, Q. Quantifying Primary and Secondary Humic-like Substances in Urban Aerosol Based on Emission Source Characterization and a Source-Oriented Air Quality Model. *Atmospheric Chemistry and Physics* **2019**, *19* (4), 2327–2341. https://doi.org/10.5194/acp-19-2327-2019.
(34) Shen, Z.; Cao, J.; Tong, Z.; Liu, S.; Reddy, L. S. S.; Han, Y.; Zhang, T.; Zhou, J. Chemical Characteristics of Submicron Particles in Winter in Xi'an. *Aerosol Air Qual. Res.* **2009**, *9* (1), 80–93. https://doi.org/10.4209/aaqr.2008.10.0050.

(35) Tan, J.; Zhang, L.; Zhou, X.; Duan, J.; Li, Y.; Hu, J.; He, K. Chemical Characteristics and Source Apportionment of PM2.5 in Lanzhou, China. *Science of The Total Environment* **2017**, *601–602*, 1743–1752. https://doi.org/10.1016/j.scitotenv.2017.06.050.
(36) Wang, S.; Yin, S.; Zhang, R.; Yang, L.; Zhao, Q.; Zhang, L.; Yan, Q.; Jiang, N.; Tang, X. Insight into the Formation of Secondary Inorganic Aerosol Based on High-Time-Resolution Data during Haze Episodes and Snowfall Periods in Zhengzhou, China. *Science of The Total Environment* **2019**, *660*, 47–56. https://doi.org/10.1016/j.scitotenv.2018.12.465.
(37) Xu, Q.; Wang, S.; Jiang, J.; Bhattarai, N.; Li, X.; Chang, X.; Qiu, X.; Zheng, M.; Hua, Y.; Hao, J. Nitrate Dominates the Chemical Composition of PM2.5 during Haze Event in Beijing, China. *Science of The Total Environment* **2019**, *689*, 1293–1303. https://doi.org/10.1016/j.scitotenv.2019.06.294.
(38) Ye, Z.; Li, Q.; Ma, S.; Zhou, Q.; Gu, Y.; Su, Y.; Chen, Y.; Chen, H.; Wang, J.; Ge, X. Summertime Day-Night Differences of PM2.5 Components (Inorganic Ions, OC, EC, WSOC, WSON, HULIS, and PAHs) in Changzhou, China. *Atmosphere* **2017**, *8* (10), 189. https://doi.org/10.3390/atmos8100189.
(39) Zhang, R.; Sun, X.; Shi, A.; Huang, Y.; Yan, J.; Nie, T.; Yan, X.; Li, X. Secondary Inorganic Aerosols Formation during Haze Episodes at an Urban Site in Beijing, China. *Atmospheric Environment* **2018**, *177*, 275–282. https://doi.org/10.1016/j.atmosenv.2017.12.031.
(40) Artaxo, P.; V. Rizzo, L.; F. Brito, J.; J. Barbosa, H. M.; Arana, A.; T. Sena, E.; G. Cirino, G.; Bastos, W.; T. Martin, S.; O. Andreae, M. Atmospheric Aerosols in Amazonia and Land Use Change: From Natural Biogenic to Biomass Burning Conditions. *Faraday Discussions* **2013**, *165* (0), 203–235. https://doi.org/10.1039/C3FD00052D.
(41) Khamkaew, C.; Chantara, S.; Janta, R.; Pani, S. K.; Prapamontol, T.; Kawichai, S.; Wiriya, W.; Lin, N.-H. Investigation of Biomass Burning Chemical Components over Northern Southeast Asia during 7-SEAS/BASELInE 2014 Campaign. *Aerosol Air Qual. Res.* **2016**, *16* (11), 2655–2670. https://doi.org/10.4209/aaqr.2016.03.0105.
(42) Kumar, V.; Rajput, P.; Goel, A. Atmospheric Abundance of HULIS during Wintertime in Indo-Gangetic Plain: Impact of Biomass Burning Emissions. *J Atmos Chem* **2018**, *75* (4), 385–398. https://doi.org/10.1007/s10874-018-9381-4.
(43) Li, J.; Song, Y.; Mao, Y.; Mao, Z.; Wu, Y.; Li, M.; Huang, X.; He, Q.; Hu, M. Chemical Characteristics and Source Apportionment of PM2.5 during the Harvest Season in Eastern China's Agricultural Regions. *Atmospheric Environment* **2014**, *92*, 442–448. https://doi.org/10.1016/j.atmosenv.2014.04.058.
(44) Pio, C. A.; Legrand, M.; Alves, C. A.; Oliveira, T.; Afonso, J.; Caseiro, A.; Puxbaum, H.; Sanchez-Ochoa, A.; Gelencsér, A. Chemical Composition of Atmospheric Aerosols during the 2003 Summer Intense Forest Fire Period. *Atmospheric Environment* **2008**, *42* (32), 7530–7543. https://doi.org/10.1016/j.atmosenv.2008.05.032.
(45) Rastogi, N.; Singh, A.; Sarin, M. M.; Singh, D. Temporal Variability of Primary and Secondary Aerosols over Northern India: Impact of Biomass Burning Emissions. *Atmospheric Environment* **2015**, *125*, 396–403. https://doi.org/10.1016/j.atmosenv.2015.06.010.
(46) Ryu, S. Y.; Kim, J. E.; Zhuanshi, H.; Kim, Y. J.; Kang, G. U. Chemical Composition of Post-Harvest Biomass Burning Aerosols in Gwangju, Korea. *Journal of the Air & Waste Management Association* **2004**, *54* (9), 1124–1137. https://doi.org/10.1080/10473289.2004.10471018.

(47) Rogula-Kozłowska, W.; Klejnowski, K. Submicrometer Aerosol in Rural and Urban Backgrounds in Southern Poland: Primary and Secondary Components of PM1. *Bull Environ Contam Toxicol* **2013**, *90* (1), 103–109. https://doi.org/10.1007/s00128-012-0868-4.
(48) Alves, C.; Pio, C.; Campos, E.; Barbedo, P. Size Distribution of Atmospheric Particulate Ionic Species at a Coastal Site in Portugal. *Quím. Nova* **2007**, *30*, 1938–1944. https://doi.org/10.1590/S0100-40422007000800027.
(49) Song, S.-K.; Shon, Z.-H.; Bae, M.-S.; Cho, S.-B.; Moon, S.-H.; Kim, H.-S.; Son, Y. B.; Lee, C. Effects of Natural and Anthropogenic Emissions on the Composition and Toxicity of Aerosols in the Marine Atmosphere. *Science of The Total Environment* **2022**, *806*, 150928. https://doi.org/10.1016/j.scitotenv.2021.150928.
(50) Xiao, H.-W.; Xiao, H.-Y.; Shen, C.-Y.; Zhang, Z.-Y.; Long, A.-M. Chemical Composition and Sources of Marine Aerosol over the Western North Pacific Ocean in Winter. *Atmosphere* **2018**, *9* (8), 298. https://doi.org/10.3390/atmos9080298.
(51) Arellanes, C.; Paulson, S. E.; Fine, P. M.; Sioutas, C. Exceeding of Henry's Law by Hydrogen Peroxide Associated with Urban Aerosols. *Environ. Sci. Technol.* **2006**, *40* (16), 4859–4866. https://doi.org/10.1021/es0513786.
(52) Wang, Y.; Arellanes, C.; Curtis, D. B.; Paulson, S. E. Probing the Source of Hydrogen Peroxide Associated with Coarse Mode Aerosol Particles in Southern California. *Environ. Sci. Technol.* **2010**, *44* (11), 4070–4075. https://doi.org/10.1021/es100593k.
(53) Xuan, X.; Chen, Z.; Gong, Y.; Shen, H.; Chen, S. Partitioning of Hydrogen Peroxide in Gas-Liquid and Gas-Aerosol Phases. *Atmospheric Chemistry and Physics* **2020**, *20* (9), 5513–5526. https://doi.org/10.5194/acp-20-5513-2020.
(54) Popovicheva, O.; Padoan, S.; Schnelle- Kreis, J.; Nguyen, D.-L.; Adam, T.; Kistler, M.; Steinkogler, T.; Kasper-Giebl, A.; Zimmermann, R.; Chubarova, N. Spring Aerosol in Urban Atmosphere of Megacity: Analytical and Statistical Assessment for Source Impacts. *Aerosol Air Qual. Res.* **2020**, *20* (4), 702–719. https://doi.org/10.4209/aaqr.2019.08.0412.
(55) Zhang, T.; Huang, S.; Wang, D.; Sun, J.; Zhang, Q.; Xu, H.; Hang Ho, S. S.; Cao, J.; Shen, Z. Seasonal and Diurnal Variation of PM2.5 HULIS over Xi'an in Northwest China: Optical Properties, Chemical Functional Group, and Relationship with Reactive Oxygen Species (ROS). *Atmospheric Environment* **2022**, *268*, 118782. https://doi.org/10.1016/j.atmosenv.2021.118782.
(56) Lin, P.; Huang, X.-F.; He, L.-Y.; Zhen Yu, J. Abundance and Size Distribution of HULIS in Ambient Aerosols at a Rural Site in South China. *Journal of Aerosol Science* **2010**, *41* (1), 74–87. https://doi.org/10.1016/j.jaerosci.2009.09.001.
(57) Wang, Y.; Hu, M.; Lin, P.; Guo, Q.; Wu, Z.; Li, M.; Zeng, L.; Song, Y.; Zeng, L.; Wu, Y.; Guo, S.; Huang, X.; He, L. Molecular Characterization of Nitrogen-Containing Organic Compounds in Humic-like Substances Emitted from Straw Residue Burning. *Environ. Sci. Technol.* **2017**, *51* (11), 5951–5961. https://doi.org/10.1021/acs.est.7b00248.
(58) Kiss, G.; Gángó, M.; Horváth, E.; Eck-Varanka, B.; Labancz, K.; Kováts, N. Assessment of Ecotoxicity of Atmospheric Humic-like Substances Using the Vibrio Fischeri Bioluminescence Inhibition Bioassay. *Atmospheric Environment* **2021**, *261*, 118561. https://doi.org/10.1016/j.atmosenv.2021.118561.
(59) Pio, C. A.; Legrand, M.; Oliveira, T.; Afonso, J.; Santos, C.; Caseiro, A.; Fialho, P.; Barata, F.; Puxbaum, H.; Sanchez-Ochoa, A.; Kasper-Giebl, A.; Gelencsér, A.; Preunkert, S.; Schock, M. Climatology of Aerosol Composition (Organic versus Inorganic) at Nonurban

Sites on a West-East Transect across Europe. *Journal of Geophysical Research: Atmospheres* **2007**, *112* (D23). https://doi.org/10.1029/2006JD008038.
(60) Nguyen, Q. T.; Kristensen, T. B.; Hansen, A. M. K.; Skov, H.; Bossi, R.; Massling, A.; Sørensen, L. L.; Bilde, M.; Glasius, M.; Nøjgaard, J. K. Characterization of Humic-like Substances in Arctic Aerosols. *Journal of Geophysical Research: Atmospheres* **2014**, *119* (8), 5011–5027. https://doi.org/10.1002/2013JD020144.
(61) Wu, D.; Li, F.; Deng, X. J.; Bi, X. Y.; Wang, X. H.; Huang, X. Y. Study on the Chemical Characteristics of Polluting Fog in Guangzhou Area in Spring. *Journal of Tropical Meteorology* **2009**, *15(1)*, 68–72.
(62) Fisak, J.; Tesar, M.; Rezacova, D.; Elias, V.; Weignerova, V.; Fottova, D. Pollutant Concentrations in Fog and Low Cloud Water at Selected Sites of the Czech Republic. *Atmospheric Research* **2002**, *64* (1), 75–87. https://doi.org/10.1016/S0169-8095(02)00081-9.
(63) Giulianelli, L.; Gilardoni, S.; Tarozzi, L.; Rinaldi, M.; Decesari, S.; Carbone, C.; Facchini, M. C.; Fuzzi, S. Fog Occurrence and Chemical Composition in the Po Valley over the Last Twenty Years. *Atmospheric Environment* **2014**, *98*, 394–401. https://doi.org/10.1016/j.atmosenv.2014.08.080.
(64) Munger, J. W.; Collett, J.; Daube, B.; Hoffmann, M. R. Fogwater Chemistry at Riverside, California. *Atmospheric Environment. Part B. Urban Atmosphere* **1990**, *24* (2), 185–205. https://doi.org/10.1016/0957-1272(90)90025-P.
(65) Cook, R. D.; Lin, Y.-H.; Peng, Z.; Boone, E.; Chu, R. K.; Dukett, J. E.; Gunsch, M. J.; Zhang, W.; Tolic, N.; Laskin, A.; Pratt, K. A. Biogenic, Urban, and Wildfire Influences on the Molecular Composition of Dissolved Organic Compounds in Cloud Water. *Atmos. Chem. Phys.* **2017**, *17* (24), 15167–15180. https://doi.org/10.5194/acp-17-15167-2017.
(66) Deguillaume, L.; Charbouillot, T.; Joly, M.; Vaïtilingom, M.; Parazols, M.; Marinoni, A.; Amato, P.; Delort, A.-M.; Vinatier, V.; Flossmann, A.; Chaumerliac, N.; Pichon, J. M.; Houdier, S.; Laj, P.; Sellegri, K.; Colomb, A.; Brigante, M.; Mailhot, G. Classification of Clouds Sampled at the Puy de Dôme (France) Based on 10 Yr of Monitoring of Their Physicochemical Properties. *Atmospheric Chemistry and Physics* **2014**, *14* (3), 1485–1506. https://doi.org/10.5194/acp-14-1485-2014.
(67) Marinoni, A.; Parazols, M.; Brigante, M.; Deguillaume, L.; Amato, P.; Delort, A.-M.; Laj, P.; Mailhot, G. Hydrogen Peroxide in Natural Cloud Water: Sources and Photoreactivity. *Atmospheric Research* **2011**, *101* (1), 256–263. https://doi.org/10.1016/j.atmosres.2011.02.013.
(68) Beiderwieden, E.; Wrzesinsky, T.; Klemm, O. Chemical Characterization of Fog and Rain Water Collected at the Eastern Andes Cordillera. *Hydrology and Earth System Sciences* **2005**, *9* (3), 185–191. https://doi.org/10.5194/hess-9-185-2005.
(69) Corell, D.; Azorin, C.; Estrela, M. J.; Valiente, J. A.; Sanz, F.; Pastor, F.; Barceló, S. Fog and Rain Water Chemistry in the Western Mediterranean Basin (Valencia Region, Spain). **2010**.
(70) Corell, D.; Estrela, M. J.; Valiente, J. A. Chemical Characterization in Coastal Fog and Rain at Mount Monduver Fog-Collection Station, Mediterranean Iberian Peninsula. *Atmospheric Research* **2021**, *258*, 105636. https://doi.org/10.1016/j.atmosres.2021.105636.
(71) Li, J.; Wang, X.; Chen, J.; Zhu, C.; Li, W.; Li, C.; Liu, L.; Xu, C.; Wen, L.; Xue, L.; Wang, W.; Ding, A.; Herrmann, H. Chemical Composition and Droplet Size Distribution of Cloud

at the Summit of Mount Tai, China. *Atmospheric Chemistry and Physics* **2017**, *17* (16), 9885–9896. https://doi.org/10.5194/acp-17-9885-2017.
(72) Vega, C. P.; Mårtensson, E. M.; Wideqvist, U.; Kaiser, J.; Zieger, P.; StrÖm, J. Composition, Isotopic Fingerprint and Source Attribution of Nitrate Deposition from Rain and Fog at a Sub-Arctic Mountain Site in Central Sweden (Mt Åreskutan). *Tellus B: Chemical and Physical Meteorology* **2019**, *71* (1), 1559398. https://doi.org/10.1080/16000889.2018.1559398.
(73) Wrzesinsky, T.; Klemm, O. Summertime Fog Chemistry at a Mountainous Site in Central Europe. *Atmospheric Environment* **2000**, *34* (9), 1487–1496. https://doi.org/10.1016/S1352-2310(99)00348-9.
(74) Watanabe, K.; Ishizaka, Y. Chemical Composition of Fog Water near the Summit of Mt. Norikura in Japan. *Journal of the Meteorological Society of Japan* **1999**, *77* (5), 997–1006.
(75) Claiborn, C. S.; Aneja, V. P. Measurements of Atmospheric Hydrogen Peroxide in the Gas Phase and in Cloud Water at Mt. Mitchell, North Carolina. *Journal of Geophysical Research: Atmospheres* **1991**, *96* (D10), 18771–18787. https://doi.org/10.1029/91JD00931.
(76) van Pinxteren, D.; Fomba, K. W.; Mertes, S.; Müller, K.; Spindler, G.; Schneider, J.; Lee, T.; Collett, J. L.; Herrmann, H. Cloud Water Composition during HCCT-2010: Scavenging Efficiencies, Solute Concentrations, and Droplet Size Dependence of Inorganic Ions and Dissolved Organic Carbon. *Atmospheric Chemistry and Physics* **2016**, *16* (5), 3185–3205. https://doi.org/10.5194/acp-16-3185-2016.
(77) Benedict, K. B.; Lee, T.; Collett, J. L. Cloud Water Composition over the Southeastern Pacific Ocean during the VOCALS Regional Experiment. *Atmospheric Environment* **2012**, *46*, 104–114. https://doi.org/10.1016/j.atmosenv.2011.10.029.
(78) Straub, D. J.; Lee, T.; Collett Jr., J. L. Chemical Composition of Marine Stratocumulus Clouds over the Eastern Pacific Ocean. *Journal of Geophysical Research: Atmospheres* **2007**, *112* (D4). https://doi.org/10.1029/2006JD007439.
(79) Hofmann, D.; Hartmann, F.; Herrmann, H. Analysis of Nitrophenols in Cloud Water with a Miniaturized Light-Phase Rotary Perforator and HPLC-MS. *Anal Bioanal Chem* **2008**, *391* (1), 161–169. https://doi.org/10.1007/s00216-008-1939-6.
(80) Richartz, H.; Reischl, A.; Trautner, F.; Hutzinger, O. Nitrated Phenols in Fog. *Atmospheric Environment. Part A. General Topics* **1990**, *24* (12), 3067–3071. https://doi.org/10.1016/0960-1686(90)90485-6.
(81) Boris, A. J.; Lee, T.; Park, T.; Choi, J.; Seo, S. J.; Collett Jr., J. L. Fog Composition at Baengnyeong Island in the Eastern Yellow Sea: Detecting Markers of Aqueous Atmospheric Oxidations. *Atmospheric Chemistry and Physics* **2016**, *16* (2), 437–453. https://doi.org/10.5194/acp-16-437-2016.
(82) Boris, A. J.; Napolitano, D. C.; Herckes, P.; Clements, A. L.; Jeffrey L. Collett, J. Fogs and Air Quality on the Southern California Coast. *Aerosol Air Qual. Res.* **2018**, *18* (1), 224–239. https://doi.org/10.4209/aaqr.2016.11.0522.
(83) Sagebiel, J. C.; Seiber, J. N. Studies on the Occurrence and Distribution of Wood Smoke Marker Compounds in Foggy Atmospheres. *Environmental Toxicology and Chemistry* **1993**, *12* (5), 813–822. https://doi.org/10.1002/etc.5620120504.
(84) Lallement, A.; Besaury, L.; Tixier, E.; Sancelme, M.; Amato, P.; Vinatier, V.; Canet, I.; Polyakova, O. V.; Artaev, V. B.; Lebedev, A. T.; Deguillaume, L.; Mailhot, G.; Delort, A.-M. Potential for Phenol Biodegradation in Cloud Waters. *Biogeosciences* **2018**, *15* (18), 5733–5744. https://doi.org/10.5194/bg-15-5733-2018.

(85) Lebedev, A. T.; Polyakova, O. V.; Mazur, D. M.; Artaev, V. B.; Canet, I.; Lallement, A.; Vaïtilingom, M.; Deguillaume, L.; Delort, A.-M. Detection of Semi-Volatile Compounds in Cloud Waters by GC×GC-TOF-MS. Evidence of Phenols and Phthalates as Priority Pollutants. *Environmental Pollution* **2018**, *241*, 616–625. https://doi.org/10.1016/j.envpol.2018.05.089.
(86) Levsen, K.; Behnert, S.; Mußmann, P.; Raabe, M.; Prieß, B. Organic Compounds In Cloud And Rain Water. *International Journal of Environmental Analytical Chemistry* **1993**, *52* (1–4), 87–97. https://doi.org/10.1080/03067319308042851.
(87) Lüttke, J.; Scheer, V.; Levsen, K.; Wünsch, G.; Neil Cape, J.; Hargreaves, K. J.; Storeton-West, R. L.; Acker, K.; Wieprecht, W.; Jones, B. Occurrence and Formation of Nitrated Phenols in and out of Cloud. *Atmospheric Environment* **1997**, *31* (16), 2637–2648. https://doi.org/10.1016/S1352-2310(96)00229-4.
(88) Lüttke, J.; Levsen, K.; Acker, K.; Wieprecht, W.; Möller, D. Phenols and Nitrated Phenols in Clouds at Mount Brocken. *International Journal of Environmental Analytical Chemistry* **1999**, *74* (1–4), 69–89. https://doi.org/10.1080/03067319908031417.
(89) Kaur, R.; Labins, J. R.; Helbock, S. S.; Jiang, W.; Bein, K. J.; Zhang, Q.; Anastasio, C. Photooxidants from Brown Carbon and Other Chromophores in Illuminated Particle Extracts. *Atmospheric Chemistry and Physics* **2019**, *19* (9), 6579–6594. https://doi.org/10.5194/acp-19-6579-2019.
(90) Smith, J. D.; Kinney, H.; Anastasio, C. Phenolic Carbonyls Undergo Rapid Aqueous Photodegradation to Form Low-Volatility, Light-Absorbing Products. *Atmospheric Environment* **2016**, *126*, 36–44. https://doi.org/10.1016/j.atmosenv.2015.11.035.